Journal of Extracellular Vesicles

RESEARCH ARTICLE OPEN ACCESS

Development of a Live-Cell Imaging Assay to Elucidate Spatiotemporal Dynamics of Extracellular Vesicle Fusion with Target Cells

Jasper van den Ende[1] | Kyra A. Y. Defourny[1] | Huib H. Rabouw[2] | Marvin E. Tanenbaum[2,3] | Richard W. Wubbolts[4] | Esther N. M. Nolte-'t Hoen[1]

[1]Division of Infection Biology, Department of Biomolecular Health Sciences, Faculty of Veterinary Medicine, Utrecht University, Utrecht, The Netherlands | [2]Oncode Institute, Hubrecht Institute-KNAW & University Medical Center Utrecht, Utrecht, The Netherlands | [3]Department of Bionanoscience, Kavli Institute of Nanoscience Delft, Delft University of Technology, Delft, The Netherlands | [4]Centre for Cell Imaging, Department of Biomolecular Health Sciences, Faculty of Veterinary Medicine, Utrecht University, Utrecht, The Netherlands

Correspondence: Esther N. M. Nolte-'t Hoen (e.n.m.nolte@uu.nl)

Received: 23 July 2025 | **Revised:** 16 December 2025 | **Accepted:** 23 December 2025

Keywords: EV-binding | EV-fusion | EV-uptake | extracellular vesicles | live-cell imaging | SunTag

ABSTRACT

Cells communicate via extracellular vesicles (EVs) containing functional RNAs, proteins, and lipids. Knowledge on the fate of internalized EVs, especially their capacity to fuse with target cell membranes and deliver luminal cargo, is limited. Currently available EV-cargo delivery assays are indirect and thus unlikely to uncover molecular players and conditions that specifically control the EV-fusion step. Here, we present a novel live-cell imaging assay for detection of EV-binding, -uptake, and -fusion in time and space. We employed the SunTag system for exceptional signal amplification. EV-donor cells were engineered to tag the luminal EV-membrane with a fluorescent label coupled to SunTag peptides. Recipient cells express fluorescent single-chain anti-SunTag antibody (STAb), which binds EV-enclosed SunTag upon its cytosolic exposure. Using SunTagged EVs carrying fusogen VSV-G, we visualize the EV-fusion process, quantify fusion kinetics and efficiency, and determine subcellular localization of fusion events. We term this methodology the Extracellular Vesicle Fusion Spatiotemporal Imaging Method (EV-FUSIM). In the future, this technology can support the identification of fusogenic EV-subsets, as well as molecular players and drugs that modulate EV-fusion, without confounding effects of post-fusion processes. This will extend knowledge on EV-biology and can aid in the engineering of EVs that efficiently deliver intraluminal therapeutic payloads.

1 | Introduction

Extracellular vesicles (EVs) are lipid-bilayer-delimited particles of ~50–500 nm released by virtually all cells across all kingdoms of life. They represent a heterogeneous mix of particles released through various biogenesis pathways. EVs contain a range of potentially functional molecules on their surface and inside their lumen, including proteins, nucleic acids, and lipids (Buck & Hoen, 2024; Van Niel et al., 2018; Welsh et al., 2024). In the past decade, EV-mediated communication has been shown to play a role in numerous (patho)physiological processes (Colombo et al., 2014; Kalluri & LeBleu, 2020). Additionally, EVs are regarded as enticing nano-vehicles for the delivery of therapeutic agents, based on their capacity to carry a range of cargos and their natural ability to modulate cellular processes (Cheng & Hill, 2022; Elsharkasy et al., 2020; Fusco et al., 2024; Herrmann et al., 2021).

Binding of EV-associated molecules to target cell receptors, either at the plasma membrane or at endosomal membranes following endocytosis and/or EV-membrane degradation, can trigger EV-induced signalling, for example, during antigen presentation (Buzas, 2023; Hirosawa et al., 2025; Van Niel et al., 2018). EV-binding and -uptake have been extensively studied, for example by using fluorescently labelled or tagged EVs combined with flow cytometry or microscopy, revealing various underlying mechanisms (Hirosawa et al., 2025; Jackson Cullison et al., 2024; Toribio et al., 2019). However, there is a long-standing debate in the field on whether and how luminal EV-cargo contributes to cytosolic signalling (Somiya, 2020). Multiple mechanisms for EV-cargo delivery to the cytosol have been proposed. Most studies argue that EVs are taken up and deliver their cargo through fusion with endosomal limiting membranes, but fusion of EVs with plasma membranes has also been suggested (Montecalvo et al., 2012; Parolini et al., 2009). Besides fusion, cargo delivery may also occur through pore formation (Soares et al., 2015; Somiya, 2020). Currently available methods for detecting cargo delivery in human and mouse target cells are largely dependent on the functional activity of transferred cargo molecules, for example, mRNA, miRNA, Cre-LoxP, CRISPR-Cas9, or split-enzyme reporters (Bittel et al., 2021; Bonsergent et al., 2021; De Jong et al., 2020; Hung & Leonard, 2016; Lai et al., 2015; Somiya & Kuroda, 2021a, 2021b; Zomer et al., 2016). Using these methods, evidence for cytoplasmic EV-mediated cargo delivery was found both *in vitro* and *in vivo*. Yet, the reported efficiency with which internalized EVs deliver functional cargo to the cytosol is generally low. For this reason, EVs designed for therapeutic cargo delivery are often equipped with viral fusion proteins, such as the vesicular stomatitis virus glycoprotein (VSV-G), to enhance their fusogenic properties (Bui et al., 2023; Ilahibaks et al., 2023; Liang et al., 2025; Ma et al., 2024; Obuchi et al., 2025; Somiya & Kuroda, 2021a, 2021b; Zhang et al., 2020). A downside of this approach is that virus-derived proteins can elicit immune reactions, which could preclude repeated dosing (Munis et al., 2019, 2020). The strong interest in optimizing current and developing novel strategies for EV-mediated therapeutic cargo delivery urges the need to increase our knowledge on how EVs are internalized and breach cellular membrane barriers to release luminal cargo into the cytoplasm.

Currently available reporter assays can provide evidence for EV-cargo delivery and illuminate parts of the underlying mechanisms, but only provide limited information on the actual EV-fusion event. Most reporter assays depend on activity-based read-outs, such as reporter activation upon genome editing by a delivered Cre-recombinase or production of bioluminescence by a reconstituted split luciferase enzyme (Bonsergent et al., 2021; Zomer et al., 2016), and are thus temporally disconnected from the actual EV-fusion event. This precludes acquisition of information on the real-time kinetics of this process. Furthermore, the reporter activity is determined by a cumulative series of events, including EV-binding, -uptake, -fusion, and the use of cargo for a functional response. Moreover, these read-outs may be sensitive to inefficient enzyme complementation, cargo degradation, or aberrant cargo localization, and tend to be spatially disconnected from the actual subcellular site of fusion. These limitations preclude the use of these reporter assays to study the efficiency and localization of discrete steps in the cascade of EV-binding, -uptake, -cargo delivery, and signalling. Attempts have been made

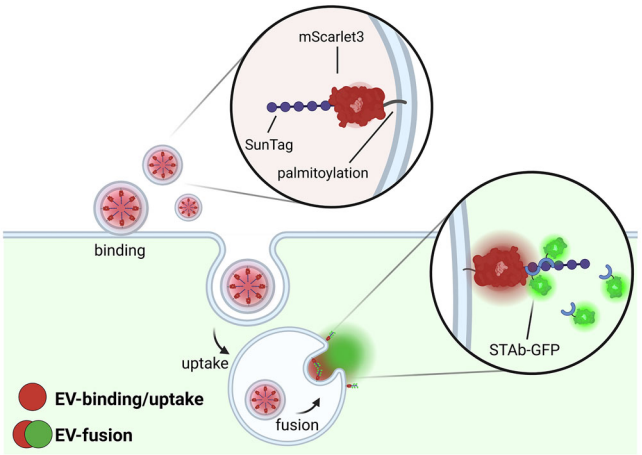

FIGURE 1 | EV-FUSIM assay principle. EV-donor cells are engineered to release EVs containing luminal red fluorescence and SunTag by lentivirally transducing them with a construct containing a palmitoylation motif, red fluorescent protein mScarlet3, and 10 repeats of the SunTag peptide. Upon addition to EV-recipient cells expressing green fluorescent anti-SunTag antibodies (STAb-GFP), EV-binding and -uptake will be visible as red fluorescent spots on and in the cells, whereas EV-fusion will result in exposure of luminal SunTag to the cytosol, thereby resulting in local concentration of STAb-GFP, visible as green spots. Created in BioRender. van den Ende, J. (2025) https://biorender.com/d7cuov7.

to directly visualize exposure of luminal EV-cargo to the cytosol of target cells using fluorescent cargo-targeting nanobodies (Joshi et al., 2020). However, this strategy only worked in cells after chemical fixation. This restricts analysis to a limited snapshot of the delivery events taking place over time and risks fixation-induced effects on the integrity of the endosomal system (Murk et al., 2003; Schnell et al., 2012; Tanaka et al., 2010). Live-cell imaging of the EV-fusion process represents an enticing alternative for visualization of EV-fusion in time and space. However, visualization of small amounts of cargo molecules exposed to the cytosol upon EV-fusion with limited laser exposure to safeguard cell viability requires exceptionally high detection sensitivity.

Here, we describe the development of a novel EV-binding, -uptake and -fusion reporter assay using state-of-the-art molecular tools and live-cell confocal microscopy (Figure 1). For detection of EV-fusion events in live cells, we adapted the SunTag system, which was originally developed for live-cell single-molecule microscopy (Tanenbaum et al., 2014) and previously used to visualize highly dynamic processes such as cellular or viral protein translation (Boersma et al., 2020; Yan et al., 2016). In order to apply this system to study EV-cell interactions, we tagged the luminal leaflet of the EV-membrane with a red fluorescent protein coupled to SunTag peptides. EV-recipient reporter cells were engineered to express green fluorescent anti-SunTag single-chain antibodies in their cytosol. Upon EV-fusion, SunTag peptides are exposed to the cytosol of recipient cells, resulting in a strong local concentration of anti-SunTag and thus a detectable increase in green fluorescence intensity, visible as green spots. Dual colour live-cell imaging of EV-recipient cells after addition of EVs isolated from EV-donor cells allows for simultaneous visualization of EV-binding and -uptake, as well

as EV-fusion, in time and space. We term this methodology Extracellular Vesicle Fusion Spatiotemporal Imaging Method (EV-FUSIM).

We first demonstrate that SunTag can be efficiently loaded with the proper orientation into HeLa cell-derived EVs. Proof-of-concept for the suitability of EV-FUSIM to visualize fusion events was obtained using HeLa cell-derived EVs mounted with VSV-G, which strongly increased fusion efficiency in both HeLa and A549 EV-recipient cells. We demonstrate that simultaneous, real-time analysis of EV-binding, -uptake, and -fusion provides the opportunity to uncouple effects of interference strategies on discrete steps in the EV-life cycle. Moreover, our data illustrate that EV-FUSIM can be used to explore the subcellular localization of EV-fusion events. This valuable addition to the EV research toolbox can assist in the identification and characterization of fusogenic EV-subsets and fusion-promoting recipient cell states, as well as in optimization of cargo delivery by therapeutic (modified) EVs.

2 | Materials and Methods

2.1 | Cells

Human cervical carcinoma (HeLa R19) and human embryonic kidney (HEK293T) cells were purchased from the American Type Culture Collection (Rockville, MD; ATCC CCL-2 and ATCC CRL-3216, respectively). HeLa STAb and A549 STAb cells, stably expressing AausFP1-STAb (denoted as STAb-GFP) and a blue fluorescent protein tagged with a nuclear localization signal (BFP-NLS), were derived from HeLa R19 and A549 cells as described previously (Boersma et al., 2020; Schipper et al., 2025; Tanenbaum et al., 2014) (STAb was originally derived from the plasmid pHR-scFv-GCN4-sfGFP-GB1-dWPRE, gift from Prof. Ron Vale—UCSF—also available as Addgene #60907). HeLa Gal3 cells, stably expressing mAG-Gal3 and BFP-NLS, were generated as described below. All cell lines were cultured in a humidified incubator at 37°C and 5% CO_2 in Dulbecco's Modified Eagle Medium (DMEM; high glucose, GlutaMAX™, Thermo Fischer Scientific, Waltham, MA, USA), supplemented with 10% fetal bovine serum (FBS; Sigma-Alrich), 100 U/mL penicillin and 100 µg/mL streptomycin (Gibco, Paisley, United Kingdom).

2.2 | Plasmids

For luminal tagging of EVs in donor cells (palm-mScar3-10xSunTag), PCR-based cloning was used to insert a fusion construct containing a palmitoylation signal sequence, mScarlet3 fluorophore (mScar3), a short GS-linker (GGGGSGGGGS), and ten repeats of the SunTag peptide, into a pHAGE2 backbone. Insert donor plasmids were: pQC palm-tdTomato (gift from Dr. Tom Driedonks, made with commercial pQC backbone, Clontech, and insert originally derived from gift pCAG PalmtdTomato plasmid described by Prof. Xandra Breakefield) (Lai et al., 2015) for the palmitoylation sequence, pN1 p3xnls-mScarlet3 (gift from Prof. Dorus Gadella—Addgene #189775) (Gadella et al., 2023) for the mScarlet3 sequence, and pcDNA4TO-UP-10xGCN4_v4-U2AF2 (generated in Tanenbaum lab) for the 10xSunTag (GCN4) sequence. For direct tagging of VSV-G, PCR-based cloning was used to insert mScar3, a GS-linker and ten repeats of the SunTag peptide, as described above, into a pCMV VSV-G plasmid (gift from Dr. Tom Driedonks, originally deposited on Addgene by Prof. Bob Weinberg—#8454) (Stewart et al., 2003). Palm-mScar3-10xSunTag and VSV-G-mScar3-10xSunTag plasmids will be made available to the community through Addgene upon publication, as #240626 and #240630, respectively.

For the generation of endolysosomal rupture reporter cells (HeLa Gal3), a pHAGE2 mAG-Gal3 plasmid (gift from Prof. Niels Geijsen—Addgene #62734) (D'Astolfo et al., 2015) for expression of mAzamiGreen-tagged Galectin-3, and a previously described pHR NLS-BFP plasmid (Boersma et al., 2020) for tagging of the nucleus with Blue Fluorescent Protein, were used.

For the generation of the mutant VSV-G expression plasmid, PCR-based cloning was used to introduce a proline-to-aspartic acid mutation at codon 127 (P127D) of the pCMV VSV-G plasmid.

2.3 | Generation of Stable Transgenic HeLa Cells

Lentiviruses were produced by co-transfection of HEK293T cells with a plasmid encoding the transgene of interest and packaging plasmids psPAX2 (gift from Dr. Tom Driedonks, originally deposited on Addgene by Prof. Didier Trono—#12260) and pCMV VSV-G into HEK293T cells using Lipofectamine 2000 (Thermo Fischer Scientific), according to the manufacturer's protocol. Supernatants were harvested 3 days after transfection, subjected to 0.45 µm filtration, and stored at −80°C until transduction. Lentivirus was supplemented with 8 µg/mL polybrene (Sigma-Aldrich) and added to HeLa R19 cells. Spin-infection was performed at 2000 rpm, 33°C for 90 min. After 3 days, transduced cells were selected using 5 µg/mL puromycin. HeLa Gal3 cells were additionally selected for high BFP and intermediate mAG fluorescence using flow cytometric sorting.

2.4 | Plasmid Transfection

Plasmid transfection was performed at approximately 70% confluency using FuGENE HD transfection reagent (Promega) according to the manufacturer's protocol, with a 3:1 reagent:DNA ratio and 80 ng (live-cell imaging in 96-well format), 500 ng (immunofluorescence in 24-well format), or 15 µg (EV isolation in T75 flask format) plasmid DNA. After overnight transfection, experiments were conducted as described below for confluent, non-transfected cell layers.

2.5 | Antibodies

The following antibodies were used for western blotting and/or immunofluorescence staining: mouse-α-CD9 (1:2000, clone HI9a; Biolegend, San Diego, CA), mouse-α-CD63 (1:500, clone Ts63; Invitrogen, MA), mouse-α-GCN4 tag (1:2000, clone C11L34; Proteogenix, France), mouse-α-VSV-G (1:2000, clone P4D5; Sigma-Aldrich), rabbit-α-Calnexin (1:1000, clone N3C2; GeneTex), HRP-coupled goat-α-mouse (1:8000, polyclonal; Sigma-Aldrich A2304), HRP-coupled goat-α-rabbit (1:10000,

polyclonal; Sigma-Aldrich A4914), AF647-coupled goat-α-mouse (1:200, polyclonal; Abcam).

2.6 | Western Blot

For analysis of cells, samples were lysed in RIPA buffer (40 mM Tris-HCl pH 8, 0.5% sodium deoxycholate, 1% Triton X-100, 150 mM sodium chloride, 0.1% sodium dodecyl sulfate) supplemented with protease inhibitor cocktail (Roche) and cleared by centrifugation at 15,000xg for 15 min. Protein concentration was determined using a Pierce BCA assay kit (Thermo Fischer Scientific) according to the manufacturer's protocol. 5 µg protein from cell lysates was mixed with Laemmli sample buffer (LSB: 62.5 mM Tris-HCl pH 6.8, 2% SDS, 10% glycerol, 0.01% bromophenol blue) with or without 20 mM 2-mercaptoethanol. For analysis of EVs within density gradient fractions, trichloroacetic acid (TCA) precipitation was performed to enable protein analysis. In brief, samples were supplemented with 125 µg/mL sodium deoxycholate and 10% ice-cold TCA, then pelleted for 15 min at 15,000xg. Pellets were washed 2x with ice-cold aceton and resuspended in LSB with or without 20 mM 2-mercaptoethanol. For analysis of purified EVs from ProtK protection experiments, samples were directly mixed with LSB. Proteins were denatured by incubating for 4 min at 98°C, separated on dodecyl sulfate-polyacrylamide gels by electrophoresis (SDS-PAGE), and transferred to 0.2 µm PVDF membranes using a Trans-Blot Turbo Transfer system (Bio-Rad). Membranes were blocked with 0.25% (v/v) fish skin gelatin (FSG; Sigma-Aldrich) in TBS + 0.1% Tween-20 (TBS-T) or 2% BSA in PBS + 0.1% Tween-20 (PBS-T) for 1 h at RT, followed by incubation o/n with primary antibodies at 4°C. Membranes were washed 5x in the appropriate blocking buffer, followed by incubation for 45 min at RT with secondary antibodies. After 3x wash in PBS-T or TBS-T, membranes were developed using Clarity Western ECL solution (BioRad) for detection on an Amersham ImageQuant 800 Imager. Imageswere processed using the ImageQuantTL software package (v10.2, Cytiva).

2.7 | Immunofluorescence Staining

After 24 h incubation with EV-depleted medium, cells grown on coverslips were washed and then fixed with 4% PFA for 15 min, washed 2x with PBS + 10 mM glycine, 1x with PBS and permeabilized for 10 min with 0.2% Triton X-100. After washing 3x with PBS + 0.1% Tween-20 (PBS-T), cells were blocked with 2% BSA in PBS-T for 1 h at RT, then stained for 45 min with primary antibodies diluted in block buffer. After three washes with PBS-T, antibody labelling was repeated with fluorophore-conjugated secondary antibodies and Hoechst 33342 (1 µg/mL, Thermo Fischer Scientific) for 30 min at RT. Finally, coverslips were washed with PBS-T and MQ before being mounted in ProLong Diamond Antifade Mountant (Thermo Fischer Scientific). Mounted slides were imaged according to specifications described below.

2.8 | EV Isolation

Confluent cell layers were washed three times with PBS +Ca +Mg and incubated with cell culture medium containing 10% EV-depleted FBS (per EV-preparation of a 100 uL, one T75 flask with 15 mL medium was used). To generate this EV-depleted FBS, FBS was prediluted 1:3 in DMEM, ultracentrifuged for 16–20 h at 28,000 rpm (100,000xg) in an SW32 rotor (k-factor 256.8) and passed through a 0.22 µm filter. 24 h after replacing the medium, cell culture supernatants were harvested and centrifuged for 10 min at 200xg and 2×10 min at 500xg to remove cells and cell debris. Cleared supernatant samples were treated with 5 mM MgCl2 and 0.1 mg/mL DNase I (Roche) for 30 min at 37°C, after which they were supplemented with 25 mM HEPES (Sigma-Aldrich). EVs were enriched from clarified supernatants by UC pelleting for 65 min at 28,000 rpm (100,000xg) in an SW32 rotor (k-factor 256.8) and resuspended in PBS +0.1% BSA (cleared from aggregates by ultracentrifugation for 16–20 h at 28,000 rpm - 100,000xg). Next, EVs were mixed with iodixanol (Optiprep; Axis-Shield, Oslo, Norway) to a final concentration of 45% and overlaid with a linear gradient of 40–5% iodixanol in PBS by adding 8 layers of 1.3 mL, decreasing in density at 5% decrements. Density gradients were centrifuged at 39,400 rpm (192,000xg) for 16 h in a SW41 rotor (k-factor 124). Gradient fractions of 1 mL were collected from the top and their densities assessed by refractometry. For experiments with purified EVs, gradient fractions 6–9 were diluted in 30 mL PBS +0.1% BSA (cleared from aggregates), isolated by UC pelleting for 90 min at 28,000 rpm in an SW32 rotor (k-factor 256.8), and resuspended in PBS.

We have submitted all relevant data regarding methodological reporting of our experiments to the EV-TRACK knowledgebase (EV-TRACK ID: EV250079) (EV-TRACK Consortium et al., 2017).

2.9 | Proteinase K Digestion

Purified EVs, isolated by UC pelleting from Optiprep density gradient fractions, were resuspended in PBS and incubated in the absence or presence of 0.2% Triton X-100 for 5 min at RT. Then, samples were incubated in the absence or presence of 45.45 ng/µL Proteinase K (Roche, Basel, Switzerland) for 1 h at 37°C. Proteinase K was inactivated by the addition of 2 mM PMSF (Roche) and subsequent incubation for 15 min on ice. Samples were mixed with LSB for SDS-PAGE and Western blot analysis.

2.10 | High Resolution Flow Cytometric Analysis of EVs

For assessment of EV distribution in Optiprep density gradients, EVs were fluorescently labelled prior to density gradient centrifugation with 30 µM CFSE (Invitrogen, Carlsbad, CA) for 60 min at RT. Individual gradient fractions 4–11 were diluted 1:20 in PBS immediately prior to high-resolution flow cytometric analysis on a Cytek Aurora spectral flow cytometer, using optimized settings for the detection of small particles, with a fluorescent threshold of 1050 in the B2 detector. A fixed volume of 20 µL of sample was measured to allow for quantitative comparison of EV release.

For normalization of purified EVs for live-cell imaging experiments, EVs isolated by UC pelleting from Optiprep density gradient fractions were resuspended in PBS. Samples were further diluted 1:400 in PBS immediately prior to flow cytometric analysis, using similar settings as described above but with an

SSC threshold of 2,000. A fixed volume of 5 µL of the samples was measured.

Data analysis for flow cytometric experiments was performed using Spectroflo v3.3.0. Background events detected in PBS were subtracted, and EV numbers in each sample were calculated based on their respective dilution factors.

Relevant data regarding methodological reporting of flow cytometry experiments have been attached as Tables S2 and S3 in the form of completed MIFlowCyt and MIFlowCyt-EV checklists, respectively (Lee et al., 2008; Welsh et al., 2020).

2.11 | Live-Cell Imaging of EV-Recipient Cells

CELLview imaging chambers (75×25 mm, glass bottom; Greiner Bio-One, The Netherlands) were seeded with EV-recipient cells one day prior to imaging in order to be confluent the next day, in 150 uL DMEM without phenol red (Thermo Fischer Scientific), supplemented with 10% FBS (Sigma-Alrich), 100 U/mL penicillin and 100 µg/mL streptomycin (Gibco). After installation on the microscope and potential drug or dye pre-treatments as described below, 100 uL medium was removed and replaced with the desired concentration of EVs pre-diluted in medium to a total volume of 100 uL, after which time-lapse imaging was immediately started as described below.

2.12 | Drug Treatments

To investigate the dependence of VSV-G-mediated EV-fusion on endolysosomal acidification, EV-recipient cells were pre-treated with 200 nM bafilomycin A1 (Cayman Chemical, Ann Arbor, MI) or DMSO vehicle control for 30 min prior to EV-addition, after which EVs were added as described above in the presence of the same concentrations of drugs. To induce endolysosomal rupture, recipient cells were treated with 1 mM L-Leucyl-L-Leucine methyl ester (hydrochloride) (LLOME; Cayman Chemical) immediately prior to live-cell imaging.

2.13 | Dye Staining

To investigate localization of EV-fusion events at endocytic compartments, EV-recipient cells were incubated with 20 nM LysoTracker-DeepRed or 5 µg/mL CellMask-DeepRed (both Invitrogen) for 15 min. After incubation, staining solution was removed and cells were washed once with medium, following EV-addition as described above.

2.14 | Microscopical Image Acquisition

Images were acquired using an Olympus SpinSR10 spinning disk confocal microscope (Evident, Leiderdorp, The Netherlands) equipped with an ORCA Fusion sCMOS camera (Hamatsu, Japan) and a 100X oil immersion objective (UPLXAPO 100XO, NA1.45; Olympus). Image recording was operated with CellSens Dimension software (v4.2) using a quadband main dichroic mirror (D405/488/561/640 nm). Hoechst/NLS-BFP were detected after 405 nm excitation using a B477/60 nm emission filter. STAb-GFP/mAzamiGreen-Gal3 were detected after 488 nm excitation using a B515/30 nm emission filter. EV-mScar3 was detected after 561 nm excitation using a B607/36 nm emission filter. AF647/LysoTracker-DeepRed/CellMask-DeepRed were detected after 640 nm excitation using a B685/40 nm emission filter.

2.15 | Live-Cell Image Acquisition Post-EV-Addition

For all experiments, Z-stacks were recorded at several randomly pre-selected positions throughout the wells of interest (minimum of three), at the time interval designated in the appropriate figure legends. For STAb and Gal3 experiments, 11 Z-slices of 1 µm step-size were recorded. For STAb localization experiments, 21 Z-slices of 0.5 µm step-size were acquired.

2.16 | Analysis of Live-Cell Imaging Experiments

Snapshot images (single Z-slices or maximum intensity projections, as denoted in figure legends) were exported from CellSens Dimension software (v4.2).

For quantitative analysis, image pre-processing was performed in FIJI (v1.54p) (Schindelin et al., 2012) to remove single pixel intensity outliers and to set the intensity range of all channels as twice the minimal intensity value in the field-of-view as minimum and 5000 as maximum. Images were median-filtered (radius = 2) and exported to a native readable h5-Imaris file format using the BigDataProcesser2 plug-in (Tischer et al., 2021). Imaris software (vs10.2; Oxford Instruments, UK) was used for further analysis in 3D, including cell segmentation and spot detection (scripts and parameters used for object creation can be found in Table S1). In brief, cells were segmented using the cell-associated STAb-GFP or mAG-Gal3 channel by creating Surface objects using the machine-learning module. Strongly bright cells were filtered out from processing to reduce false positive STAb/Gal3 spot detection. Subsequently, EV-mScar3 and STAb spots were segmented using the Spot detection module. Spots were filtered based on the distance to the created cell Surface objects to exclude non-cell-associated spots. For EV-mScar3 spots, an additional classification was performed based on the distance to the cell Surface to differentiate plasma membrane-proximal and -distal spots, in order to differentially quantify EV-binding and -uptake. Object counts for STAb or Gal3 spots, EV-mScar3 total spots, EV-mScar3 PM-proximal spots and EV-mScar3 PM-distal spots, as well as the sum volume of cell objects, were exported per timepoint for each field-of-view and further analysed in Excel (v2408; Microsoft, US). Average sum cell volumes/field-of-view were calculated for HeLa STAb, A549 STAb and HeLa Gal3 datasets (131970.7, 127732.8 and 111537.98 μm^3/FOV, respectively), after which all spot counts were corrected for the difference between the associated sum cell volume and the calculated average, in order to correct for differences in cell coverage and occasional focus losses. Maximum corrected spot counts within the full time-lapse for each field-of-view were used for bar graphs and statistical comparison between conditions.

2.17 | Localization Analyses

For LysoTracker- and CellMask-DeepRed channels, images were subjected to additional background subtraction (radius = 0.3 μm) in Imaris, after which Surface objects were segmented in these channels using absolute intensity thresholding. For NLS-BFP channels, Surface objects were created using the machine-learning module. For all three, binary masks were generated from these Surface objects to use in the classification of overlapping STAb spots. Cell Surface objects and STAb spots were segmented as described above. As a threshold for overlap, we chose a minimum of 25% overlap of STAb spot and localization binary masks. We determined the average STAb spot object volume in the localization dataset to be 1.96 μm^3, corresponding to 928 voxels (with dimensions of 0.065 × 0.065 × 0.5 μm each). Thus, a minimum of 25% overlap corresponds to 232 voxels. As each positive voxel in the binary masks has an intensity of 1, a summed intensity of 232 in the masked channel was used as a threshold to designate a spot as an overlapping event. Average sum cell volumes/field-of-view were calculated for the STAb localization dataset (122418.73 μm^3/FOV), and used for correction of spot counts as described above.

2.18 | Statistical Analysis

Statistical analysis and data plotting were performed using Prism (10.0; GraphPad Software). Statistical tests used are denoted in the appropriate figure legends.

2.19 | Table-of-Contents Graphical Abstract

Created in BioRender. van den Ende, J. (2025) https://biorender.com/8ihhtg1.

3 | Results

3.1 | Engineering of Donor Cells for Production of SunTagged EVs

In order to simultaneously detect EV-binding/uptake and -fusion upon addition to recipient cells, we developed a strategy to tag the lumen of EVs released by mammalian cells with a red fluorescent protein and SunTag peptides (Figure 1). By implementing a repeating array of SunTag peptides, small amounts of cargo molecules exposed to the cytosol upon EV-fusion can be detected by multiple fluorescently labelled single-chain anti-SunTag antibodies (STAb-GFP) per tagged molecule, facilitating strong signal amplification. To achieve this, we generated cervical epithelial HeLa EV-donor cells stably expressing mScarlet3 and 10 repeats of SunTag linked to a palmitoylation motif (HeLa palm-mScar3-10xST), a proven strategy for tagging the inner leaflet of the EV-membrane (Lai et al., 2015). Microscopic imaging of these cells confirmed expression and colocalization of mScarlet3 and SunTag, predominantly at the plasma membrane (Figure 2A). EVs released by these cells were isolated from cell culture supernatants using differential (ultra)centrifugation followed by density gradient centrifugation (Figure 2B). Immunoblot analysis confirmed that SunTag co-fractionated with EV-associated tetraspanins CD9 and CD63 in fractions 6–9 of the density gradient (Figure 2C). SunTag was detected as two bands, with the top band running near the expected size of the full-length palm-mScar3-10xSunTag construct (55.75 kDa). The additional lower band likely resulted from hydrolysis of mScar3, as previously shown for dsRed-like fluorescent proteins in denaturing conditions (Gross et al., 2000; McCullock et al., 2020). In line with this, the lower band was relatively more abundant in samples processed by strongly denaturing TCA precipitation (Figures 2C and 3B) than in non-precipitated samples (Figures 2E and 3D) (Koontz, 2014). SunTag-containing fractions 6–9, with densities of 1.04–1.10 g/mL, contained the highest number of EVs as assessed by high resolution flow cytometry (Figures S1A–**C**). To prove the luminal orientation of EV-associated SunTag, we tested the pooled EV fractions (1.04–1.10 g/mL) for protection of SunTag from Proteinase K (ProtK), which digests externally accessible EV proteins but leaves those protected by the EV-membrane intact (Figure 2D). Indeed, ProtK treatment did not lead to SunTag digestion unless the EV-membrane was disrupted with the detergent Triton X-100, while CD9 was also cleaved by ProtK in the absence of detergent (Figure 2E). Based on these data, we conclude that engineered EV-donor cells release EV-associated SunTag with the correct membrane orientation.

Incorporation of fusogenic viral glycoprotein VSV-G is a proven tool for enhancing cytosolic delivery of luminal EV-cargo (Bui et al., 2023; Ilahibaks et al., 2023; Liang et al., 2025; Ma et al., 2024; Obuchi et al., 2025; Somiya & Kuroda, 2021a, 2021b; Zhang et al., 2020). Thus, we incorporated VSV-G in our system in order to generate EVs with high fusogenic potential. EVs from control-transfected cells were included to control for potential effects of transfection on the endosomal system (Pemberton et al., 2024) and EV-release and -functionality, as well as to rule out effects of contaminating transfection complexes in EV-preparations (McCann et al., 2022). Transfection of palm-mScar3-10xST EV-donor cells with VSV-G resulted in colocalization of palm-mScar3-10xST and VSV-G at the plasma membrane (Figure 3A). Released VSV-G co-fractionated with CD9, CD63, and SunTag (Figure 3B). VSV-G transfection led to a shift of EVs containing CD9/63 and SunTag to slightly higher densities (1.08–1.13 g/mL) when compared to EVs from control-transfected cells (Figure 3B). Additionally, CD63 was detected at a lower molecular weight in both cell lysates and EVs from VSV-G-transfected cells, suggesting altered glycosylation. In line with previous reports (Bui et al., 2023; Ilahibaks et al., 2023), VSV-G transfection led to a strong increase in total EV release, as measured with high-resolution flow cytometry (Figures 3C and S2), and by immunoblotting for CD9 and SunTag (Figure 3D). VSV-G transfection did not alter the orientation of EV-associated palm-mScar3-10xST, as demonstrated by ProtK protection assays (Figure 3D). Together, these data demonstrate that transfection of EV-donor cells with VSV-G induces the release of VSV-G-containing SunTagged EVs. We used these EV-isolates to further develop our EV-FUSIM live-cell imaging assay.

3.2 | EV-FUSIM Simultaneously Traces EV-Binding, -Uptake, and -Fusion in Live Cells

EV-recipient cells were engineered to express cytosolic anti-SunTag single-chain antibodies coupled to a bright green

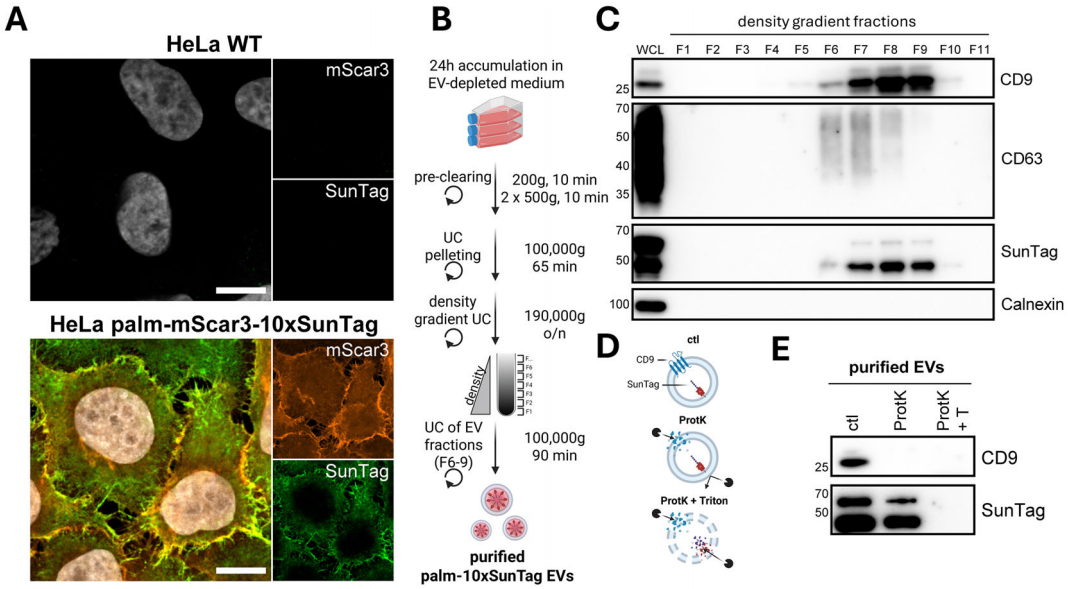

FIGURE 2 | HeLa palm-mScar3-10xST cells release luminally SunTagged EVs. (A) HeLa WT and palm-mScar3-10xST cells fixed after 24 h incubation in EV-depleted medium and immunolabelled for SunTag. Images shown are mid-nuclear Z-slices, showing fluorescence for mScar3 (red), SunTag (green), and Hoechst-labelled nuclei (white). Scale bars represent 10 μm. Images are representative of $n = 2$ independent experiments. (B) Schematic overview of EV-isolation methodology. See Materials & Methods for a detailed description. Created in BioRender. van den Ende, J. (2025) https://biorender.com/hvvdrpk. (C) EV-containing ultracentrifugation pellets from HeLa palm-mScar3-10xST cells were floated into iodixanol density gradients, after which individual gradient fractions were concentrated using TCA precipitation and analysed for the presence of protein markers by Western blotting. (D) Schematic overview of the Proteinase K protection assay principle. See Materials & Methods for a detailed description. Created in BioRender. van den Ende, J. (2025) https://BioRender.com/pb45em2. (E) Gradient-purified EVs were treated with ProtK in the absence or presence of 0.2% Triton X-100 and analysed by Western blotting. For SunTag, two bands are visible, corresponding to a full-length construct (top) and a fragmented version (bottom), which is likely the result of denaturation in the Western blot procedure (see Materials & Methods for detailed explanation).

fluorescent protein (AausFP1 (Lambert et al., 2020), denoted as STAb-GFP from here onwards). EV-FUSIM requires that cytosolic exposure of SunTag upon EV-fusion locally concentrates STAb-GFP in recipient cells, which can be detected as fluorescent spots using live cell imaging. Direct transfection of HeLa cells stably expressing STAb-GFP with the SunTag construct, thereby bypassing the EV-fusion process, confirmed recruitment of STAb-GFP to mScar3-positive sites at the plasma membrane (Figure S3). Next, we tested the suitability of this system for live-cell imaging of EV-binding/uptake and -fusion (Figure 4A). EVs were purified from HeLa palm-mScar3-10xST donor cells as described before and quantified using high-resolution flow cytometry. Purified EVs were added to HeLa STAb-GFP recipient cells, after which time-lapse imaging was immediately initiated. Images were acquired from multiple positions per well, capturing Z-stacks with red- and green-channel fluorescence from each position at a time interval of 1 h. Here, we treated 4×10^4 recipient cells with a low (1×10^8, 2500/cell) or high (5×10^8, 12500/cell) dose of EVs, as well as a low dose of transfection control or VSV-G EVs. In all EV-treated conditions but not the medium control, cell-associated red fluorescent (mScar3+) spots accumulated over time, indicating binding and/or uptake of EVs (Figures 4B and S4A). Only for VSV-G EVs, this was also associated with an accumulation of green fluorescent (GFP+) spots, indicating EV-fusion, predominantly at early timepoints (Figures 4B and S4B).

For in-depth quantitative analysis of EV-binding/uptake and -fusion, we designed a 3D image analysis pipeline (Figure 5A). Following image pre-processing, cell boundaries were detected and segmented in 3D, after which cell-associated fluorescent spots were detected in both channels and counted (see Materials & Methods for detailed description). Incubation of cells with EVs led to time- and dose-dependent accumulation of EV-binding/uptake (Figure 5B, C). For VSV-G EVs, the EV-binding/uptake efficiency was strongly increased. Quantitative image analysis confirmed that EV-fusion was detected exclusively for VSV-G EVs (Figure 5D, E). For EVs lacking VSV-G, neither a higher dose nor prolonged incubation significantly increased the detection of green fluorescent spots compared to the medium control. To separately investigate EV-binding and -uptake, we quantified red fluorescent spots based on their distance to the surface of the segmented cell volumes (Figure S5A, B). Both cell surface-bound and internalized EVs could be detected in these experiments, ruling out that a lack of EV-fusion detection is due to a lack of EV-uptake into the endosomal system (Figure S5C–E). For VSV-G EVs, green fluorescent spots were detected immediately after the start of imaging and increased in number up to the first hour after addition of EVs (Figure 5D, E). Beyond this timepoint, the detection of fusion events plateaued and eventually dissipated. Further corroborating efficient exposure of SunTag to the cytosol from VSV-G-containing palm-SunTag EVs, we observed a relative depletion of STAb-GFP signal from the nucleus, which is a known proxy for STAb sequestration in the cytosol (Figure S6A–C) (Khuperkar et al., 2020). At later timepoints, we observed an increase of plasma membrane-associated fluorescence, which precluded confident spot detection beyond 4 h after EV-addition (Figure S4B). The observed disappearance

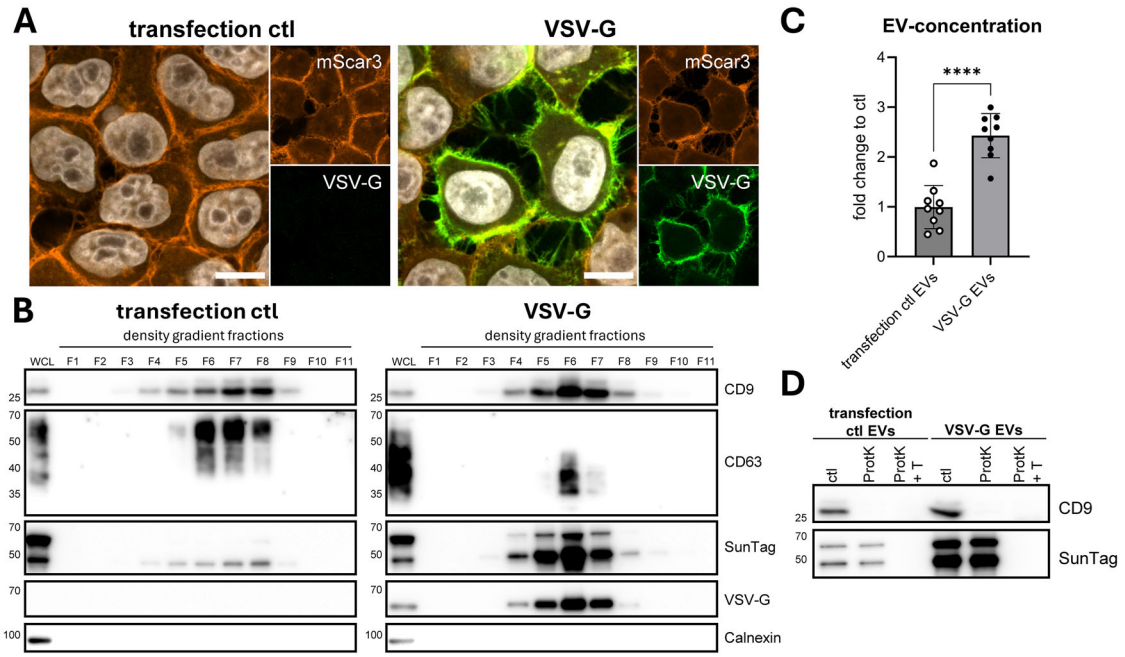

FIGURE 3 | Transfection of HeLa palm-mScar3-10xST cells with VSV-G results in release of VSV-G-containing SunTagged EVs. (A) Mock- or VSV-G-transfected HeLa palm-mScar3-10xST cells were fixed after overnight transfection followed by 24 h incubation in EV-depleted medium, then immunolabelled for VSV-G. Images shown are mid-nuclear Z-slices, showing fluorescence for mScar3 (red), VSV-G (green) and Hoechst-labelled nuclei (white). Scale bars represent 10 μm. Images are representative of $n = 2$ independent experiments. (B) EV-containing ultracentrifugation pellets from mock- and VSV-G-transfected cells were floated into iodixanol density gradients, after which individual gradient fractions were concentrated using TCA precipitation and analysed for the presence of protein markers by Western blotting. (C) EV-concentrations in gradient-purified EV preparations isolated from mock- and VSV-G-transfected cells were quantified using high resolution flow cytometry. Graph shows the mean fold change to transfection ctl EVs ± SD, calculated from $n = 8$ independent experiments. **** $p \leq 0.0001$ as determined by paired t-test. (D) Gradient-purified EVs isolated from mock- and VSV-G-transfected cells were treated with ProtK in the absence or presence of 0.2% Triton X-100 and analysed by Western blotting. For SunTag, two bands are visible, corresponding to full-length construct (top) and a fragmented version (bottom) which is likely the result of denaturation in the Western blot procedure (see Materials & Methods for detailed explanation).

of STAb concentrates from EV-fusion locations and redistribution to the plasma membrane is likely due to de-palmitoylation which frequently occurs in the cytosol (Kathayat & Dickinson, 2019), and may be followed by re-palmityolation and insertion in the plasma membrane (Figure S6D, E). To validate the results in a different recipient cell type, we treated A549 alveolar epithelial cells expressing STAb-GFP with HeLa palm-mScar3-10xST transfection ctl or VSV-G EVs. Similar to HeLa recipient cells, cell-associated red fluorescent spots accumulated over time in EV-treated conditions, with a higher binding/uptake efficiency for VSV-G EVs (Figure S7A–**C**). Only for VSV-G EVs, green fluorescent EV-fusion spots were observed, with fusion kinetics similar to those observed in HeLa recipient cells (Figure S7A,D,E). Thus, EV-FUSIM readily detects EV-binding, -uptake and VSV-G-mediated EV-fusion in live cells over prolonged periods of imaging, allowing for quantitative assessment of each of these processes.

3.3 | Real-Time Visualization of EV-Fusion Events

The data in Figure 5 indicate that VSV-G-mediated EV-fusion has fast kinetics, peaking as early as 1 h post-EV-addition. Therefore, we next used EV-FUSIM to assess EV-binding/uptake and -fusion kinetics at higher temporal resolution, by imaging cells every 15 min up to 2 h after EV-addition (Video **S1**). Even at these early timepoints, cell-associated red spots accumulated much more rapidly in cells treated with VSV-G EVs compared to control EVs (Figure 6A–C). In cells treated with VSV-G-EVs but not control EVs, green spot detection increased from 15 to 60 min after addition of EVs, after which a plateau was reached (Figure 6A,D,E). Furthermore, imaging at a 1-min interval allowed for visualization of EV-fusion events in real-time, with red-fluorescent spots eventually turning red-green positive upon EV-fusion (Figure 6F). Thus, EV-FUSIM allows for assessment of fusion kinetics. Down-titration of the VSV-G EV dose indicated that both EV-binding/uptake and -fusion remained detectable down to an added dose of 5×10^6 (125 EVs/cell) (Figure S8). To exclude that the observed STAb-GFP concentrates were the result of endo-lysosomal rupture rather than fusion events, we used an established Galectin-3 reporter assay in parallel live-cell imaging experiments (Figure 9A). Galectin-3 is a small cytosolic molecule that clusters on permeabilized endosomes by binding β-galactosides present on the inner leaflet of the endosomal membrane (D'Astolfo et al., 2015). HeLa cells were transduced to express Galectin 3 tagged with green fluorophore mAzamiGreen (HeLa mAG-Gal3) and used as EV-recipient cells in our live-cell imaging setup. Treatment with VSV-G EVs did not lead to an increase in green spots compared to untreated cells despite efficient EV-binding/uptake by the HeLa mAG-Gal3 reporter cells (Figures 6G–I, and S9B–D). As a positive control, we used L-leucyl-L-leucine methyl ester (LLOMe). This polymer, described

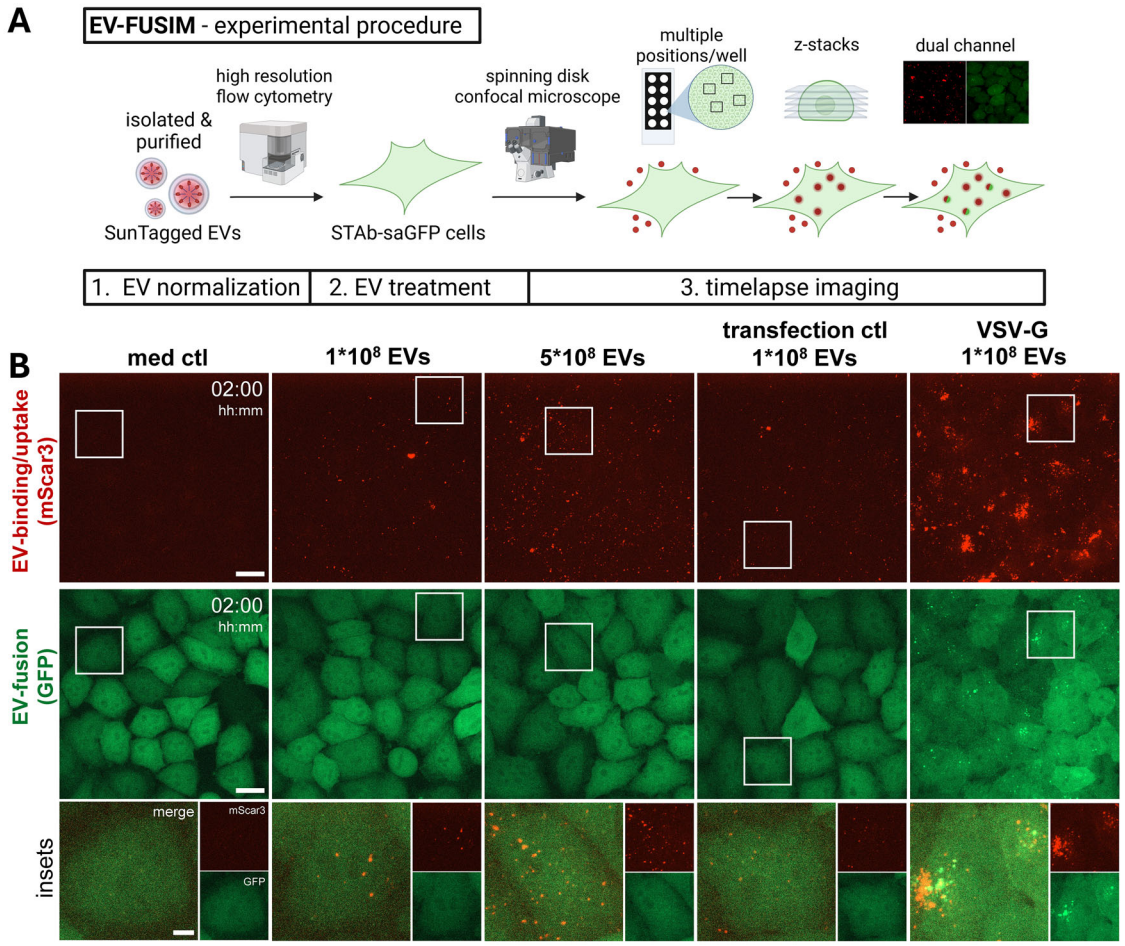

FIGURE 4 | Live-cell imaging of HeLa STAb-GFP cells after addition of SunTagged EVs allows for tracing of EV-binding/uptake and -fusion over time. (A) Schematic overview of live-cell imaging procedure. See Materials & Methods for a detailed description. Created in BioRender. van den Ende, J. (2025) https://BioRender.com/gaf5kzg. (B) Live HeLa STAb-GFP cells were subjected to time-lapse imaging immediately after the addition of medium only or medium containing the indicated concentrations and types of EVs, taking Z-stacks at a 1 h time interval. Images are maximum intensity projections acquired at 2 h post-EV-addition, showing fluorescence channels for mScar3 (top) and GFP (middle) in the same fields-of-view. Gamma was adjusted to 2 (mScar3) or 1.2 (GFP) for visualization purposes only. Scale bars represent 20 μm. White insets correspond to magnifications (bottom), which show mScar3, GFP, and merged channels. Scale bar represents 5 μm. Images are representative of $n = 3–4$ independent experiments.

to permeabilize endo-lysosomes, rapidly induced accumulation of intracellular green spots (Figure 6G–I). Thus, VSV-G-mediated EV-cargo delivery occurs through fusion of EV- and target cell membranes, rather than endo-lysosomal rupture. Taken together, these data show that EV-FUSIM facilitates real-time, simultaneous assessment of EV-binding/uptake and -fusion of VSV-G EVs with unprecedented sensitivity and temporal resolution.

3.4 | EV-FUSIM an Disentangle Mechanisms Controlling EV-Binding/Uptake or EV-Fusion

Based on the capacity of EV-FUSIM to simultaneously detect EV-binding, -uptake and -fusion, we tested whether this technology can be used to disentangle factors that specifically control discrete steps in this cascade. In order to modulate the capacity of recipient cells to support EV-fusion, we treated HeLa STAb recipient cells with V-ATPase inhibitor Bafilomycin A1 (BafA1). BafA1 is known to abrogate the pH-dependent fusogenic capacity of VSV-G, both in the context of infection with bona fide VSV (Burkard et al., 2014) and for VSV-G-containing EVs (Somiya & Kuroda, 2021b), by preventing endosomal acidification. Treatment with BafA1 prior to addition of EVs affected neither binding nor uptake of VSV-G EVs, did not affect the binding/uptake of VSV-G EVs, as indicated by the lack of a significant difference in red spot detection compared to vehicle control-treated cells (Figures 7A–C and S10A). In contrast, BafA1 completely abrogated the detection of fusion events, as evidenced by a reduction of green spot detection to levels observed for cells which were not incubated with EVs (Figure 7A,D,E). Thus, inhibition of endolysosomal acidification specifically abrogates VSV-G-mediated EV-fusion, without affecting upstream EV-binding and -uptake. Complementary to this approach, we tested whether genetic ablation of the fusogenic capacity of VSV-G reduced the detection of fusion events with EV-FUSIM. Hereto, we introduced the P127D mutation into VSV-G, which has been described to disrupt fusogenic capacity without affecting receptor binding (Fredericksen & Whitt, 1995; Liang et al., 2025). Similar to wild-type VSV-G, VSV-G P127D colocalized with mScar3 at the plasma membrane (Figure S11A) and co-fractionated with CD9, CD63 and SunTag in density gradients

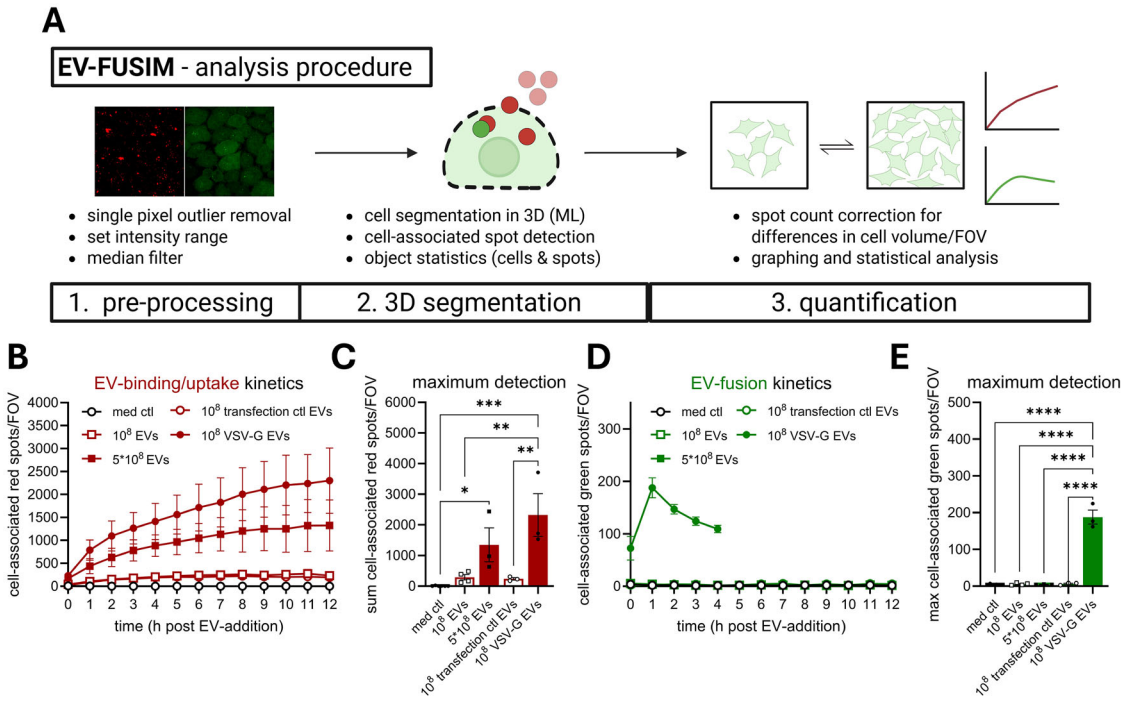

FIGURE 5 | Image analysis with 3D cell segmentation facilitates quantitative assessment of EV-binding/uptake and -fusion. (A) Schematic overview of image analysis procedure. See Materials & Methods for a detailed description. Created in BioRender. van den Ende, J. (2025) https://BioRender.com/k3ijxlv. (B–E) After segmentation of cells in 3D based on the GFP channel, cell-associated fluorescent spots in the red and green channels were counted for each field-of-view. In tandem, the total cell volume per field-of-view was counted, which was used to correct spot counts for differences from the average cell volume per field-of-view. Graphs show the corrected mean spots per timepoint (B, D) or mean maximum spot detection over the course of the experiment (C, E) per field-of-view for both mScar3 and GFP channels ± SEM, calculated from $n = 3$-4 independent experiments with 3–6 fields-of-view per condition each. For all experimental conditions, quantification was performed for all timepoints, except for GFP spots in the VSV-G EV condition, where only the first 4 h were processed, as changes in membrane fluorescence after this timepoint precluded proper spot detection. * $p \leq 0.05$, ** $p \leq 0.01$, *** $p \leq 0.001$, and **** $p \leq 0.0001$ as determined by one-way ANOVA with Tukey's multiple comparisons test.

upon release (Figure S11B). (Figures 3B, and S11B). Furthermore, this VSV-G mutant retained its capacity to strongly induce EV-release, as measured with high-resolution flow cytometry (Figure S11C). Upon addition to HeLa STAb recipient cells, VSV-G WT and P127D EVs exhibited similar binding/uptake efficiency, as indicated by a strong increase in red spot detection compared to cells treated with control EVs (Figures 8A–C and S10B). Conversely, only VSV-G WT EVs resulted in significant detection of fusion events, while treatment with VSV-G P127D EVs did not result in significant green spot detection (Figure 8A,D,E). Thus, introduction of the P127D mutation in VSV-G results in loss of EV-fusion, while maintaining efficient EV-binding and -uptake. Together, these data illustrate that perturbations in the EV-fusion process that occur independent of EV-binding and -uptake can be quantitatively analysed using EV-FUSIM. This opens up unique opportunities to delineate the specific mechanisms underlying EV-binding, -uptake and -fusion.

3.5 | Subcellular Localization of EV-Fusion Events by Colocalizing with Compartments of Interest

Precise subcellular locations of EV-fusion remain poorly understood. We reasoned that the spatial resolution offered by EV-FUSIM could aid in understanding at which types of membranes VSV-G EVs fuse. Plasma membranes and endosomes originating from them were labelled with CellMask, while acidic late endosomes and lysosomes were labelled with Lysotracker (Figure 9A) (Barral et al., 2022; Jenkins et al., 2015). These staining procedures did not negatively affect EV-fusion, indicated by similar numbers and kinetics of EV-fusion events in dye-stained and unstained HeLa STab recipient cells (Figure S12). Next, the occurrence of EV-fusion events at the stained subcellular compartments was assessed based on fluorescent intensity measurements in the segmented 3D STAb-GFP objects (see Materials & Methods for detailed description). EV-fusion events occurred at the plasma membrane and/or endosomes, as the vast majority of fusion spots were detected at CellMask-stained compartments, particularly at early timepoints (Figure 9B). A decrease in the percentage of fusion spots labelled by CellMask was observed at later timepoints, which is likely a consequence of dye depletion as internalization from the plasma membrane progresses. In contrast, EV-fusion events rarely occurred at acidic late endosomes or lysosomes across the course of the experiment, as evidenced by infrequent spot detection at LysoTracker-stained compartments (Figure 9C). Indeed, the fraction of EV-fusion events occurring at the plasma membrane and/or endosomes was significantly higher than that occurring at acidic compartments (Figure 9D). By differentially segmenting CellMask-positive EV-fusion events based on their proximity to the cell surface,

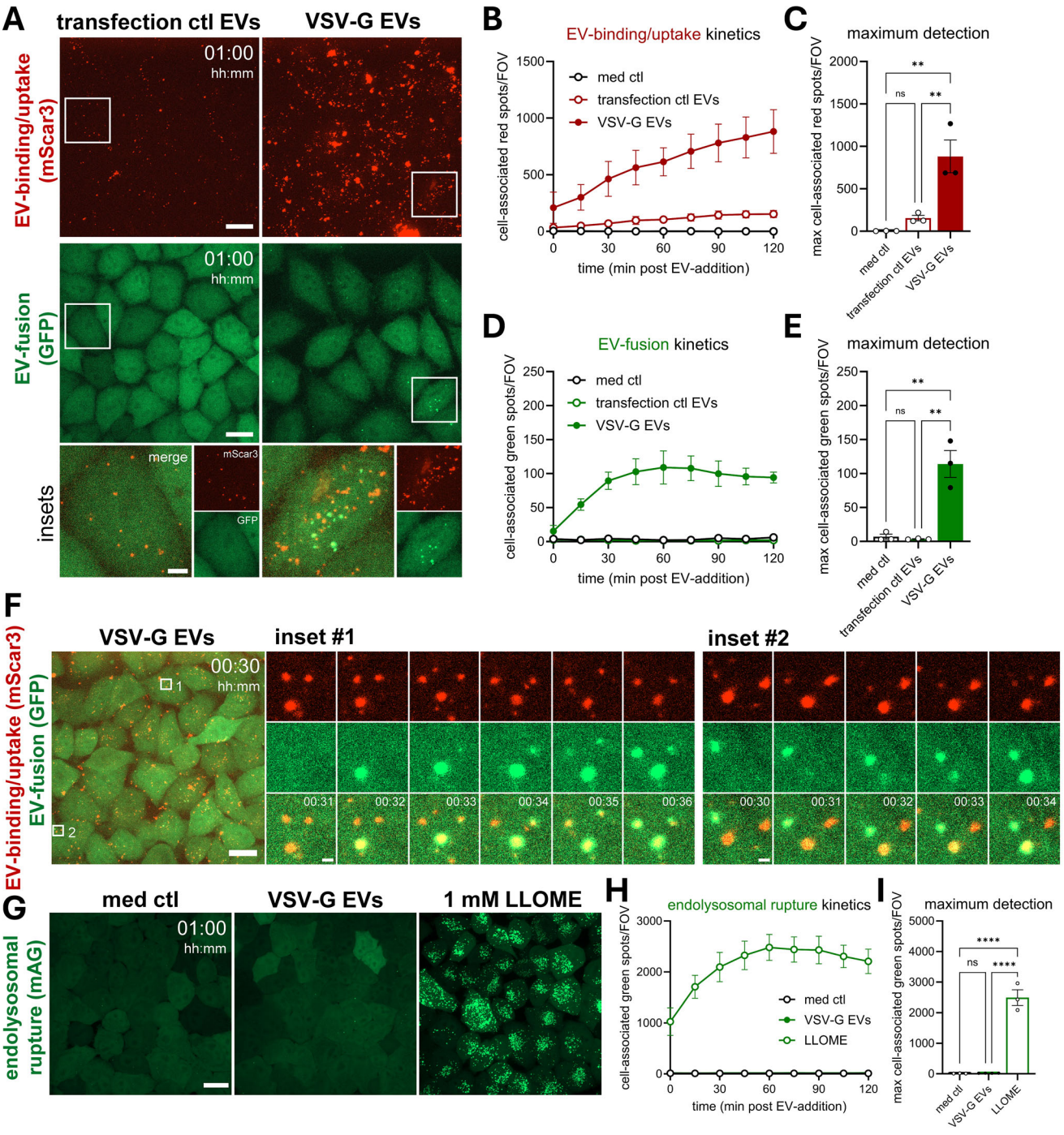

FIGURE 6 | Legend on next page.

we could further confirm that the vast majority of EV-fusion events occurred at internalized endosomal membranes, not at the plasma membrane (Figure 9E). Together, these data indicate that VSV-G EVs preferentially fuse at early, less acidic endosomal compartments.

The subcellular location where EVs deliver their cargo may influence the likelihood that bioactive molecules contained in EVs reach their site of action. The nucleus has been suggested as an important site of action for cargo delivered by both EVs and viruses (Corbeil et al., 2020; Santos et al., 2021, 2023). EV-FUSIM offers the opportunity to assess whether the actual fusion process takes place in the proximity of specific target organelles. We used our localization analysis pipeline to differentially classify spots overlapping with a blue fluorescent protein tagged to a nuclear localization signal (NLS-BFP), to assess the proximity of EV-fusion events to the nucleus. Interestingly, a large fraction of EV-fusion events overlapped with NLS-BFP, indicating close proximity to the nucleus (Figure 10A). Nucleus-proximal EV-fusion was a stable constituent of the total EV-fusion process over time, representing approximately 33.7% of the total detected events (Figure 10B, C). This indicates VSV-G EVs can fuse with endosomal membranes in very close proximity to the nuclear envelope, potentially delivering cargo in a favor-

able location for transport into the nucleus. Combined, our data illustrate that the high spatio-temporal resolution of EV-FUSIM offers ample opportunities to unravel previously unexplored aspects of the EV-fusion process, including subcellular localization.

4 | Discussion

Detailed mechanistic understanding of EV-target cell interactions is a pre-requisite for exploring the role of EVs in (patho)physiological processes, modulating their functional properties, and ultimately harnessing them for therapeutic approaches. Here, we extended the EV-toolbox by developing an Extracellular Vesicle Fusion Spatiotemporal Imaging Method (EV-FUSIM)—a methodology for live-cell imaging of EV-binding, -uptake and -fusion with target cells in time and space.

We engineered EV-donor cells to tag the luminal EV-membrane with red fluorescent proteins coupled to SunTag peptides using a palmitoylation motif (Figure 2). Additional VSV-G expression in donor cells induced the release of SunTagged, VSV-G-containing EVs (Figure 3). Upon addition of SunTagged EVs to recipient cells expressing anti-SunTag single-chain antibodies, we were able to detect EV-binding and -uptake across different EV-concentrations and conditions in real-time for prolonged periods (Figures 4 and 5). For VSV-G EVs, we were additionally able to detect EV-fusion in live cells (Figures 4 and 5). By imaging at short time intervals, we provide real-time visualization of EV-fusion with recipient cell membranes (Figure 6). Using chemical inhibition of endosomal acidification as well as mutagenesis of VSV-G, we demonstrate that simultaneous detection of EV-binding, -uptake, and -fusion in real-time facilitates the disentanglement of distinct steps in the EV-target cell interaction cascade (Figures 7 and 8). Lastly, localization analysis can be combined with EV-FUSIM to determine where in the endosomal system EV-fusion occurs, and which cellular organelles are in close proximity to the EV-fusion event could thus be targets of the delivered EV-cargo (Figures 9 and 10). Thus, we have developed a comprehensive methodology capable of determining kinetics, relative efficiency, and subcellular localization of EV-binding, -uptake, and -fusion.

Using EV-FUSIM, we were able to comprehensively characterize the interactions of VSV-G EVs with target cells in time and space. Firstly, we demonstrate that VSV-G increases the binding and uptake efficiency of EVs (Figures 4–6). Similar observations have been made previously using bioluminescent reporters or flow cytometry (Bui et al., 2023; Stranford et al., 2023) and could be linked to binding of the viral glycoprotein to its widely expressed cellular receptor, LDLR, thereby inducing its internalization (Finkelshtein et al., 2013). Secondly, we show that VSV-G-mediated EV-fusion occurs rapidly, with STAb-GFP spots visible immediately after the start of imaging and maxing out between 30 and 60 min after addition of EVs (Figures 4–6). These rapid fusion kinetics are in line with previous reports demonstrating this for both VSV-G-containing EVs and bona fide VSV, using bioluminescent and fluorescence resonance energy transfer (FRET) reporters, respectively. (Cabot et al., 2022; Somiya & Kuroda, 2021a). The fusion detection plateau we observe after 60 min could reflect a technical limitation of the system. It is possible that at these later timepoints the VSV-G-containing EVs still internalize and fuse, but can no longer be detected due to saturation of the limited amount of STAb-GFP molecules in recipient cells. Alternatively, the pool of EVs containing VSV-G may internalize and fuse rapidly at early timepoints, whereas SunTagged EVs without VSV-G on their surface may internalize with slower kinetics but do not have the capacity to fuse. Thirdly, we provide novel evidence that the mechanism of VSV-G-mediated EV-cargo delivery is via EV-fusion, rather than endolysosomal rupture (Figure 6). To further substantiate this conclusion, we show that recipient cell endosomal acidification and the proline amino acid at position 127 of VSV-G are cru-

FIGURE 6 | EV-FUSIM facilitates real-time visualization of VSV-G-mediated EV-fusion. (A) Live HeLa STAb-GFP cells were subjected to time-lapse imaging immediately after addition of medium only or medium containing 10^8 transfection ctl or VSV-G EVs, taking Z-stacks at a 15 min time interval. Images are maximum intensity projections acquired at 1 h post-EV-addition, showing fluorescence channels for mScar3 (top) and GFP (middle) in the same fields-of-view. Gamma was adjusted to 2 (mScar3) or 1.2 (GFP) for visualization purposes only. Scale bars represent 20 μm. White insets correspond to magnifications (bottom), which show mScar3, GFP and merged channels. Scale bar represents 5 μm. Images are representative of $n = 3$ independent experiments. (B–E) After segmentation of cells in 3D based on the GFP channel, cell-associated fluorescent spots in the red and green channels were counted for each field-of-view. In tandem, the total cell volume per field-of-view was counted, which was used to correct spot counts for differences to the average cell volume per field-of-view. Graphs show the corrected mean spots per timepoint (B, D) or mean maximum spot detection over the course of the experiment (C, E) per field-of-view for both mScar3 and GFP channels ± SEM, calculated from n = 3 independent experiments with 2–6 fields-of-view per condition each. * $p \leq 0.05$, ** $p \leq 0.01$ and *** $p \leq 0.001$ as determined by one-way ANOVA with Tukey's multiple comparisons test. (F) Live HeLa STAb-GFP were subjected to time-lapse imaging 30 min after addition of medium containing 10^8 VSV-G EVs, taking Z-stacks at a 1 min time interval. Images are representative of $n = 2$ independent experiments. Overview image is a maximum intensity projection of the start of the experiment, showing a merge of fluorescence channels for mScar3 and GFP. Scale bar represents 20 μm. Insets shown in white correspond to magnified images of single EV-containing endosomes on the right, showing fluorescence channels for mScar3, GFP and a merge of both at the indicated timepoints post-EV-addition. Scale bars represent 1 μm. (G) Live HeLa mAG-Gal3 cells were subjected to time-lapse imaging immediately after addition of medium only, medium containing 10^8 VSV-G EVs or medium containing 1 mM LLOME, taking Z-stacks at a 15 min time interval. Images are maximum intensity projections acquired at 1 h post-EV-addition, showing the fluorescence channel for mAG. Gamma was adjusted to 1.2 (mAG) for visualization purposes only. Scale bar represents 20 μm. (H, I) After segmentation of cells in 3D based on the mAG channel, cell-associated fluorescent spots in the green channel were counted for each field-of-view. In tandem, the total cell volume per field-of-view was counted, which was used to correct spot counts for differences to the average cell volume per field-of-view. Graph shows the corrected mean spots per timepoint (H) or mean maximum spot detection over the course of the experiment (I) per field-of-view for the mAG channel ± SEM, calculated from $n = 3$ independent experiments with 5–6 fields-of-view per condition each. **** $p \leq 0.0001$ as determined by one-way ANOVA with Tukey's multiple comparisons test.

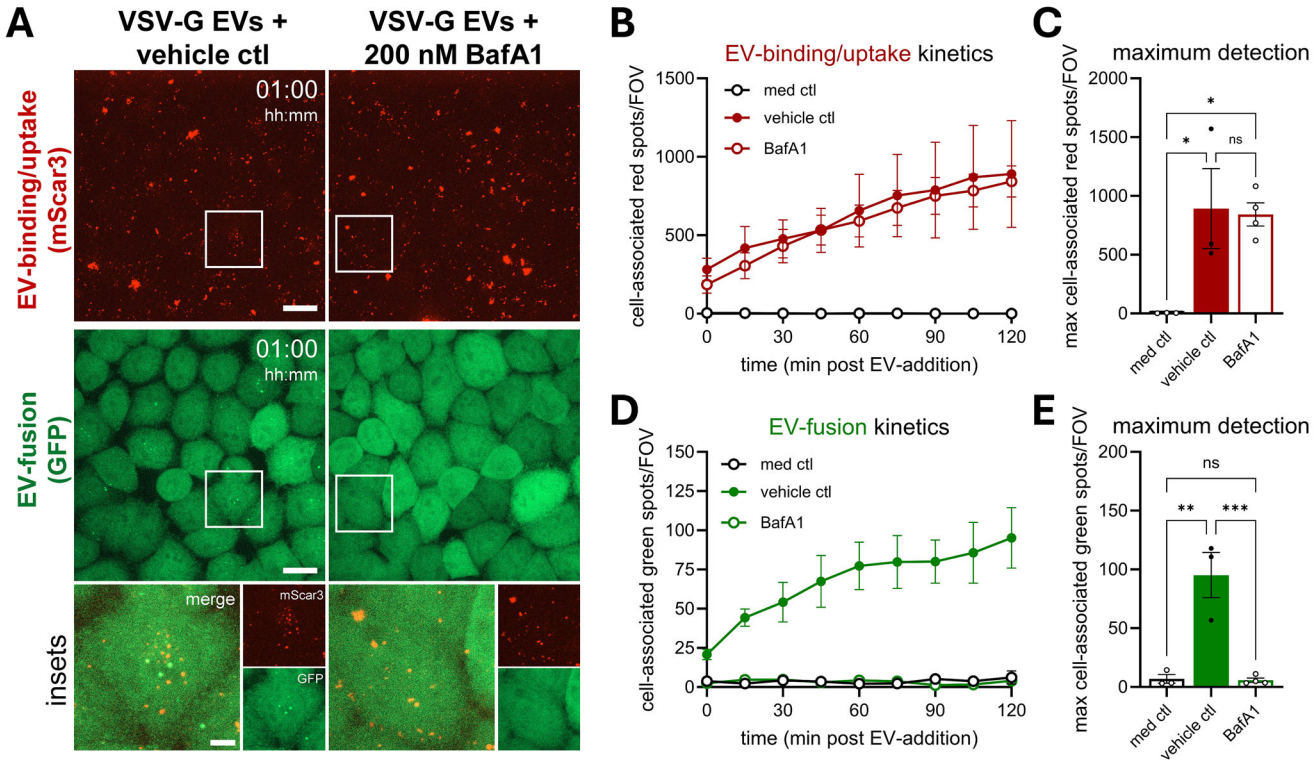

FIGURE 7 | Inhibition of endosomal acidification specifically abrogates VSV-G-mediated EV-fusion without affecting EV-binding/uptake. (A) Live HeLa STAb-GFP cells were pre-treated with DMSO (vehicle ctl) or Bafilomycin A1 for 30 min, followed by addition of medium containing 10^8 VSV-G EVs in the continued presence of the compounds, then immediately subjected to time-lapse imaging, taking Z-stacks at a 15 min time interval. Images are maximum intensity projections acquired at 1 h post-EV-addition, showing fluorescence channels for mScar3 (top) and GFP (middle) in the same fields-of-view. Gamma was adjusted to 2 (mScar3) or 1.2 (GFP) for visualization purposes only. Scale bars represent 20 μm. White insets correspond to magnifications (bottom), which show mScar3, GFP, and merged channels. Scale bar represents 5 μm. Images are representative of $n = 3$–4 independent experiments. (C–E) After segmentation of cells in 3D based on the GFP channel, cell-associated fluorescent spots in the red and green channels were counted for each field-of-view. In tandem, the total cell volume per field-of-view was counted, which was used to correct spot counts for differences to the average cell volume per field-of-view. Graphs show the corrected mean spots per timepoint (B, D) or mean maximum spot detection over the course of the experiment (C, E) per field-of-view for both mScar3 and GFP channels ± SEM, calculated from $n = 3$-4 independent experiments with 2–6 fields-of-view per condition each. * $p \leq 0.05$, ** $p \leq 0.01$, and *** $p \leq 0.001$ as determined by one-way ANOVA with Tukey's multiple comparisons test.

cial factors in determining fusion efficiency (Figures 7 and 8). Furthermore, we demonstrate that fusion of VSV-G EVs occurs predominantly in early, less acidic endosomes, rather than in late endosomes or lysosomes (Figure 9). This is in line with previous studies showing fusion-promoting conformational changes in VSV-G occur at slightly acidic pH values (around 6.2) using in vitro liposome fusion assays or FRET-based pH sensors (Cabot et al., 2022; Kim et al., 2017). Such pH values occur early in the endosomal system (Wang et al., 2017). Lastly, we observed that a substantial fraction of VSV-G-mediated EV-fusion events occurs in close proximity to the nucleus (Figure 10). Migration of the viral G-protein to the nucleus during VSV infection was reported nearly three decades ago, although the implications for virus infection remained underexplored (Da Poian et al., 1996). Our data suggest that VSV-G EVs could be transported through the endosomal system to a similar location, and eventually fuse near the nuclear envelope. Many therapeutically relevant EV-cargoes, such as Cas9-gRNA complexes, need to reach the nucleus for their activity. Nucleus-proximal EV-fusion might be beneficial or even required for functional delivery of such cargoes, by minimizing their presence in the cytosol, where there is a potential risk of degradation and/or inactivation. Altogether, exploration of the fundamental mechanisms of VSV-G-mediated EV-cargo delivery as described here could prove invaluable in the development of novel and optimization of current VSV-G EV-based therapeutics. Real-time detection of distinct steps in the delivery pathways, as facilitated by EV-FUSIM, can in the future be used to assess the effects of, for example, VSV-G mutants or drugs, in order to ultimately improve functional cargo delivery. In addition, it may allow for successful reiteration of gain-of-function screens exploring alternative EV-fusion factors, which have thus far been largely inconclusive (Liang et al., 2025).

The live-cell imaging data we present here substantiate previous findings that the efficiency of EV-mediated cargo delivery is generally low (De Jong et al., 2020; Ilahibaks et al., 2023; Liang et al., 2025; Obuchi et al., 2025). EV-FUSIM recipient cells never showed a significant increase in green fusion spot detection when exposed to EVs lacking VSV-G, even when treated with 12,500 EVs/cell and followed for 12 h (Figures 4 and 5). EVs released via different biogenesis pathways or by diverse cell types exhibit strong differences in molecular cargo, and may

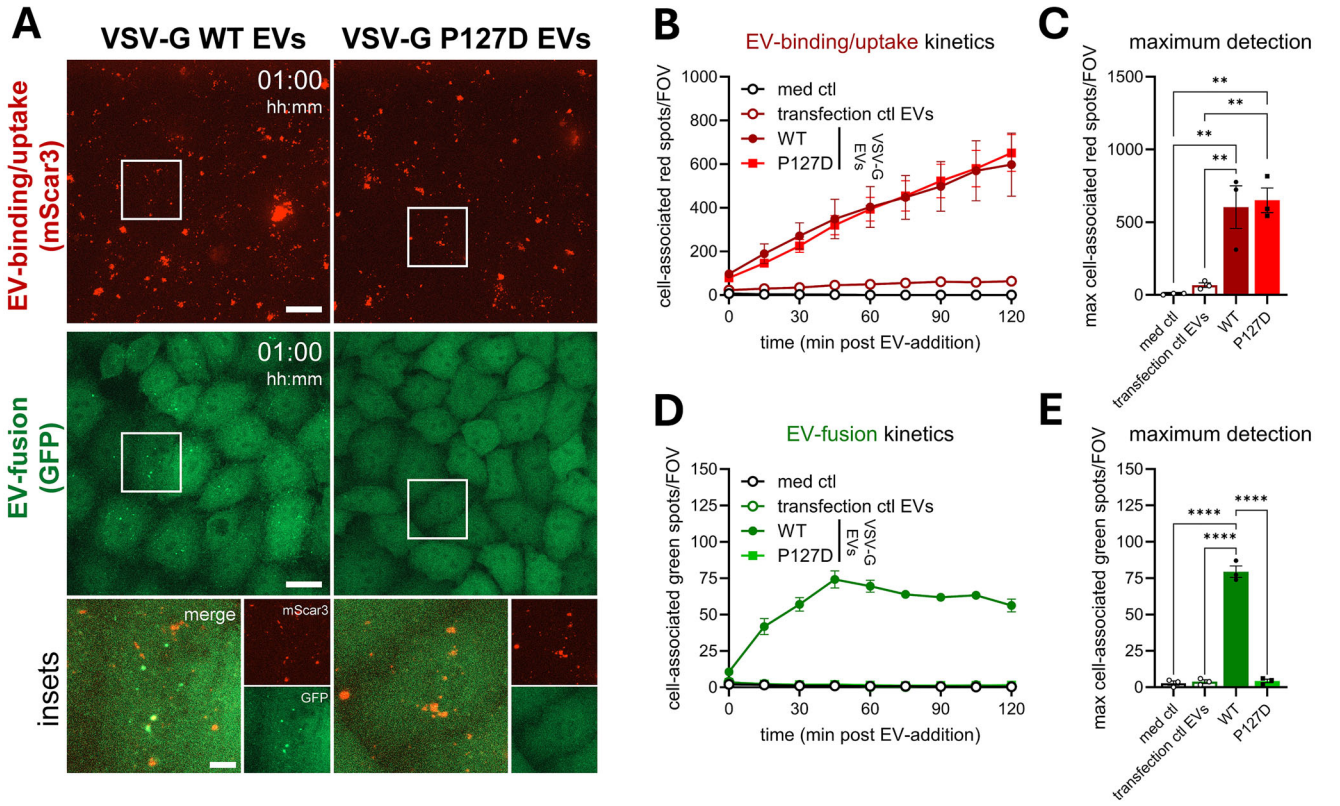

FIGURE 8 | Introduction of the P127D mutation in VSV-G abrogates VSV-G-mediated EV-fusion without affecting EV-binding/uptake. (A) Live HeLa STAb-GFP cells were subjected to time-lapse imaging immediately after addition of medium only or medium containing 108 transfection ctl, VSV-G WT or VSV-G P127D EVs, taking Z-stacks at a 15 min time interval. Images are maximum intensity projections acquired at 1 h post-EV-addition, showing fluorescence channels for mScar3 (top) and GFP (middle) in the same fields-of-view. Gamma was adjusted to 2 (mScar3) or 1.2 (GFP) for visualization purposes only. Scale bars represent 20 μm. White insets correspond to magnifications (bottom), which show mScar3, GFP and merged channels. Scale bar represents 5 μm. Images are representative of $n = 3$ independent experiments. (B–E) After segmentation of cells in 3D based on the GFP channel, cell-associated fluorescent spots in the red and green channels were counted for each field-of-view. In tandem, the total cell volume per field-of-view was counted, which was used to correct spot counts for differences to the average cell volume per field-of-view. Graphs show the corrected mean spots per timepoint (B, D) or mean maximum spot detection over the course of the experiment (C, E) per field-of-view for both mScar3 and GFP channels ± SEM, calculated from $n = 3$ independent experiments with 3–4 fields-of-view per condition each. ** $p \leq 0.01$ and **** $p \leq 0.0001$ as determined by one-way ANOVA with Tukey's multiple comparisons test.

therefore also differ in fusogenic capacity. In this study, we used a palmitoylation motif to tag EVs through general membrane labelling, which likely captures a wide spectrum of EVs released via different biogenesis pathways. Indeed, mScarlet3 was detected on both the plasma membrane and internal compartments upon expression of the construct in HeLa cells (Figure 2). Our data indicate that EVs released by HeLa cells do not fuse with HeLa or A549 target cells under the specified conditions at an efficiency high enough to detect in our assay. Nevertheless, we cannot rule out that these cells release specific subsets of highly fusogenic EVs which are either not tagged using our strategy or exhibit a fusion frequency that is lower than the throughput of our assay. In the future, mScar3-SunTag tagging of marker proteins present in specific EV-subsets combined with strategies to enrich for tagged subsets could address such limitations (Bobbili et al., 2024; Obuchi et al., 2025). More research is also needed to assess the suitability of EV-FUSIM to track cytosolic exposure of particularly low-abundant EV-cargo molecules. In addition, it is important to note that absolute quantification of EV-fusion efficiency is precluded in the current experimental set-up, because the limited resolution of confocal fluorescent microscopy makes it impossible to distinguish individual EVs from clusters on cells and inside endosomes. Advances in SunTag-compatible super-resolution techniques such as single-molecule localization microscopy could aid in detection of single EV-fusion events in the future (Castells-Garcia et al., 2021). Finally, it is crucial to implement and optimize the use of EV-FUSIM in primary cell cultures and *in vivo* systems, in order to explore EV-fusion in more physiological contexts. Previous implementation of SunTag-based imaging systems in organoids and several model organisms (including Drosophila and Zebrafish) corroborates the feasibility of applying EV-FUSIM in such contexts (Boersma et al., 2020; Liu et al., 2023; Pizzey et al., 2025). The lack of data on whether and how EV-fusion is influenced by donor and recipient cell types, culture conditions, EV-tagging and -isolation methodologies, as well as reporter assays constitutes a major knowledge gap in the EV research field. Our novel technology offers the opportunity for direct real-time detection of EV-fusion with target cells to explore

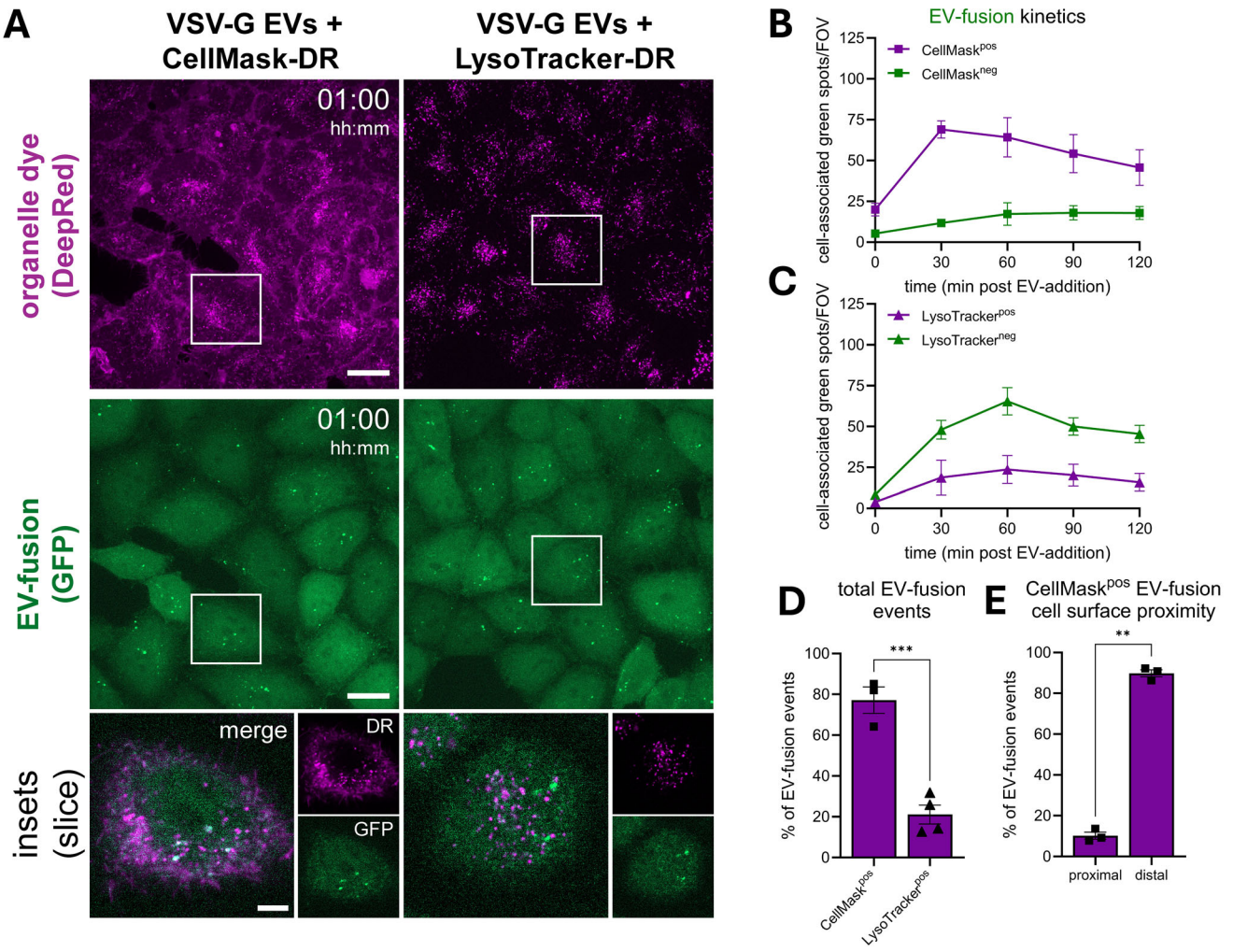

FIGURE 9 | Localization analysis suggests VSV-G-mediated EV-fusion occurs predominantly in early endosomes. (A) Live HeLa STAb-GFP cells were left untreated or stained for 15 min with either 20 nM LysoTracker-DeepRed or 5 μg/mL CellMask, washed with medium followed by addition of 10^8 VSV-G EVs, then immediately subjected to time-lapse imaging, taking Z-stacks at a 30 min time interval. Overview images are maximum intensity projections acquired at 1 h post-EV-addition, showing fluorescence channels for DeepRed (top) and GFP (middle) in the same fields-of-view. Gamma was adjusted to 1.2 (DeepRed and GFP) for visualization purposes only. Scale bars represent 20 μm. White insets correspond to single Z-slice magnifications (bottom), which show DeepRed, GFP, and merged channels. Scale bar represents 5 μm. Images are representative of n = 3-4 independent experiments. (B, C) After segmentation of cells in 3D based on the GFP channel, cell-associated fluorescent spots in the green channel were counted for each field-of-view and differentially classified as dye-negative or -positive, based on a threshold of at least 25% of the mean STAb spot volume staining positive. In tandem, the total cell volume per field-of-view was counted, which was used to correct spot counts for differences to the average cell volume per field-of-view. Graphs show the corrected mean spots per timepoint, per class ± SEM, calculated from $n = 3$–4 independent experiments with 4–6 fields-of-view per condition each. (D) Graph shows the mean percentage of the total GFP spots staining positive for each dye ± SEM, based on the cumulative spots over 2 h per field-of-view and calculated from $n = 3$–4 independent experiments with 4–6 fields-of-view per condition each. *** $p \leq 0.001$ as determined by unpaired *t*-test. (E) CellMask-positive GFP spots were further sub-classified based on their distance to the segmented cell surface, as proximal (<500 nm) or distal (>500 nm). Graph shows the mean percentage of the total CellMask-positive GFP spots in either class ± SEM, based on the. data shown before ** $p \leq 0.01$ as determined by paired *t*-test.

the influence of these variables without confounding effects of post-fusion processes.

In conclusion, an increased appreciation in the field of the tightly regulated nature of EV-fusion with target cells calls for methods that directly and specifically assess fusion efficiency with high spatiotemporal precision. The EV-FUSIM system, which we have described here, can be utilized in the future to identify fusogenic EV-subsets, fusion-promoting recipient cell types or states, and molecular players involved in these processes. Although viral fusion proteins can enhance fusion of engineered EVs, their immunogenicity is a clear disadvantage for therapeutic use. This calls for the discovery of novel fusogenic moieties or EV-fusion-enhancing drugs for use in the clinic. Being able to monitor and understand the fusion step in the EV-life cycle will be instrumental for the engineering of vesicles that efficiently deliver

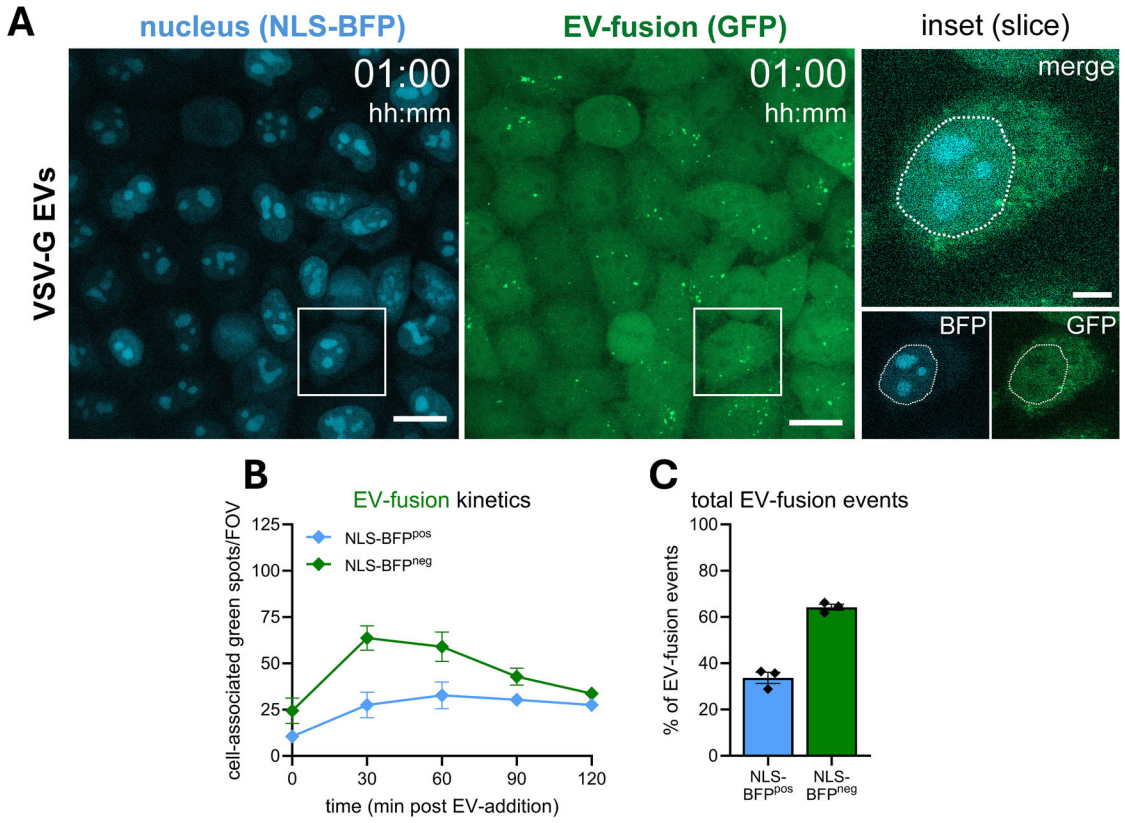

FIGURE 10 | A substantial fraction of VSV-G-mediated EV-fusion events occurs in close proximity to the nucleus. (A) Live HeLa STAb-GFP cells expressing a nuclear localization signal-tagged BFP were subjected to time-lapse imaging immediately after addition of medium containing 10^8 VSV-G EVs, taking Z-stacks at a 30 min time interval. Overview images are maximum intensity projections acquired at 1 h post-EV-addition, showing fluorescence channels for BFP (left) and GFP (right) in the same fields-of-view. Gamma was adjusted to 1.2 (BFP and GFP) for visualization purposes only. Scale bars represent 20 μm. White insets correspond to single Z-slice magnifications (right), which show BFP, GFP and merged channels. Scale bar represents 5 μm. White dashed line indicates nuclear outline, drawn for visualization purposes only. Images are representative of $n = 3$ independent experiments. (B) After segmentation of cells in 3D based on the GFP channel, cell-associated fluorescent spots in the green channel were counted for each field-of-view and differentially classified as BFP-negative or –positive, based on a threshold of at least 25% of the mean STAb spot volume staining positive. In tandem, the total cell volume per field-of-view was counted, which was used to correct spot counts for differences to the average cell volume per field-of-view. Graph shows the corrected mean spots per timepoint, per class ± SEM, calculated from $n = 3$ independent experiments with 6 fields-of-view each. (C) Graph shows the mean percentage of the total GFP spots staining positive for BFP ± SEM, based on the cumulative spots over 2 h per field-of-view and calculated from $n = 3$ independent experiments with 6 fields-of-view each.

intraluminal therapeutic payloads at the desired subcellular location.

Author Contributions

Jasper van den Ende: conceptualization, formal analysis, investigation, methodology, writing – original draft, writing – review and editing. **Kyra A.Y. Defourny**: conceptualization, methodology. **Huib H. Rabouw**: methodology. **Marvin E. Tanenbaum**: conceptualization. **Richard W. Wubbolts**: conceptualization, formal analysis, methodology, supervision, writing – review and editing. **Esther N. M. Nolte-'t Hoen**: conceptualization, funding acquisition, supervision, writing – review and editing.

Acknowledgements

We are grateful to the Centre for Cellular Imaging Utrecht and the Flow Cytometry and Cell Sorting Facility, both at the Faculty for Veterinary Medicine of Utrecht University, for allowing access to their facilities, training and support. We thank dr. Pieter Vader (UMC Utrecht) for providing an antibody targeting Calnexin. This work also received support from COST Action CA20110 'RNA communication across kingdoms: new mechanisms and strategies in pathogen control (exRNA-PATH)', supported by COST (European Cooperation in Science and Technology).

Funding

This work was supported by The Netherlands Organisation for Scientific Research under Grants NWO-VICI VI.C.212.072 and NWO-XS OCENW.XS23.1.151 awarded to E.N.M.N-'tH. The funders had no role in study design, data collection and analysis, decision to publish, or preparation of the manuscript.

Conflicts of Interest

Dr. Nolte-'t Hoen is an editor with the Journal of Extracellular Vesicles and has played no part in the peer review of this manuscript.

Data Availability Statement

The authors confirm that the data supporting the findings are available within the article or its supplementary material. Raw data that support the findings presented here can be made available upon reasonable request. We have submitted all relevant data regarding methodological reporting of our experiments to the EV-TRACK knowledgebase (EV-TRACK ID: EV250079) (EV-TRACK Consortium et al., 2017). Relevant data regarding methodological reporting of flow cytometry experiments has been attached as Supplementary Tables 2 and 3 in the form of completed MIFlowCyt and MIFlowCyt-EV checklists, respectively (J. A. Lee et al., 2008; Welsh et al., 2020).

References

Barral, D. C., L. Staiano, C. Guimas Almeida, et al. 2022. "Current Methods to Analyze Lysosome Morphology, Positioning, Motility and Function." *Traffic (Copenhagen, Denmark)* 23, no. 5: 238–269. https://doi.org/10.1111/tra.12839.

Bittel, M., P. Reichert, I. Sarfati, et al. 2021. "Visualizing Transfer of Microbial Biomolecules by Outer Membrane Vesicles in Microbe-Host-Communication In Vivo." *Journal of Extracellular Vesicles* 10, no. 12: e12159. https://doi.org/10.1002/jev2.12159.

Bobbili, M. R., A. Görgens, Y. Yan, et al. 2024. "Snorkel-Tag Based Affinity Chromatography for Recombinant Extracellular Vesicle Purification." *Journal of Extracellular Vesicles* 13, no. 10: e12523. https://doi.org/10.1002/jev2.12523.

Boersma, S., H. H. Rabouw, L. J. M. Bruurs, et al. 2020. "Translation and Replication Dynamics of Single RNA Viruses." *Cell* 183, no. 7: 1930–1945.e23. https://doi.org/10.1016/j.cell.2020.10.019.

Bonsergent, E., E. Grisard, J. Buchrieser, O. Schwartz, C. Théry, and G. Lavieu. 2021. "Quantitative Characterization of Extracellular Vesicle Uptake and Content Delivery Within Mammalian Cells." *Nature Communications* 12, no. 1: 1864. https://doi.org/10.1038/s41467-021-22126-y.

Buck, A. H., and E. N. M. N. Hoen. 2024. "The Nature and Nurture of Extracellular Vesicle' Mediated Signaling." *Annual Review of Genetics* 58: 409–432. https://doi.org/10.1146/annurev-genet-111523-102725.

Bui, S., J. Dancourt, and G. Lavieu. 2023. "Virus-Free Method to Control and Enhance Extracellular Vesicle Cargo Loading and Delivery." *ACS Applied Bio Materials* 6, no. 3: 1081–1091. https://doi.org/10.1021/acsabm.2c00955.

Burkard, C., L.-M. Bloyet, O. Wicht, et al. 2014. "Dissecting Virus Entry: Replication-Independent Analysis of Virus Binding, Internalization, and Penetration Using Minimal Complementation of β-Galactosidase." *PLoS ONE* 9, no. 7: e101762. https://doi.org/10.1371/journal.pone.0101762.

Buzas, E. I. 2023. "The Roles of Extracellular Vesicles in the Immune System." *Nature Reviews Immunology* 23, no. 4: 236–250. https://doi.org/10.1038/s41577-022-00763-8.

Cabot, M., V. Kiessling, J. M. White, and L. K. Tamm. 2022. "Endosomes Supporting Fusion Mediated by Vesicular Stomatitis Virus Glycoprotein Have Distinctive Motion and Acidification." *Traffic (Copenhagen, Denmark)* 23, no. 4: 221–234. https://doi.org/10.1111/tra.12836.

Castells-Garcia, A., I. Ed-daoui, E. González-Almela, et al. 2021. "Super Resolution Microscopy Reveals How Elongating RNA Polymerase II and Nascent RNA Interact With Nucleosome Clutches." *Nucleic Acids Research* 50, no. 1: 175–190. https://doi.org/10.1093/nar/gkab1215.

Cheng, L., and A. F. Hill. 2022. "Therapeutically Harnessing Extracellular Vesicles." *Nature Reviews Drug Discovery* 21, no. 5: 379–399. https://doi.org/10.1038/s41573-022-00410-w.

Colombo, M., G. Raposo, and C. Théry. 2014. "Biogenesis, Secretion, and Intercellular Interactions of Exosomes and Other Extracellular Vesicles." *Annual Review of Cell and Developmental Biology* 30, no. 1: 255–289. https://doi.org/10.1146/annurev-cellbio-101512-122326.

Corbeil, D., M. F. Santos, J. Karbanová, T. Kurth, G. Rappa, and A. Lorico. 2020. "Uptake and Fate of Extracellular Membrane Vesicles: Nucleoplasmic Reticulum-Associated Late Endosomes as a New Gate to Intercellular Communication." *Cells* 9, no. 9: 1931. https://doi.org/10.3390/cells9091931.

Da Poian, A. T., A. M. Gomes, R. J. Oliveira, and J. L. Silva. 1996. "Migration of Vesicular Stomatitis Virus Glycoprotein to the Nucleus of Infected Cells." *Proceedings of the National Academy of Sciences* 93, no. 16: 8268–8273. https://doi.org/10.1073/pnas.93.16.8268.

D'Astolfo, D. S., R. J. Pagliero, A. Pras, et al. 2015. "Efficient Intracellular Delivery of Native Proteins." *Cell* 161, no. 3: 674–690. https://doi.org/10.1016/j.cell.2015.03.028.

De Jong, O. G., D. E. Murphy, I. Mäger, et al. 2020. "A CRISPR-Cas9-Based Reporter System for Single-Cell Detection of Extracellular Vesicle-Mediated Functional Transfer of RNA." *Nature Communications* 11, no. 1: 1113. https://doi.org/10.1038/s41467-020-14977-8.

Elsharkasy, O. M., J. Z. Nordin, D. W. Hagey, et al. 2020. "Extracellular Vesicles as Drug Delivery Systems: Why and How?" *Advanced Drug Delivery Reviews* 159: 332–343. https://doi.org/10.1016/j.addr.2020.04.004.

Finkelshtein, D., A. Werman, D. Novick, S. Barak, and M. Rubinstein. 2013. "LDL Receptor and Its family Members Serve as the Cellular Receptors for Vesicular Stomatitis Virus." *Proceedings of the National Academy of Sciences* 110, no. 18: 7306–7311. https://doi.org/10.1073/pnas.1214441110.

Fredericksen, B. L., and M. A. Whitt. 1995. "Vesicular Stomatitis Virus Glycoprotein Mutations That Affect Membrane Fusion Activity and Abolish Virus Infectivity." *Journal of Virology* 69, no. 3: 1435–1443. https://doi.org/10.1128/jvi.69.3.1435-1443.1995.

Fusco, C., G. De Rosa, I. Spatocco, et al. 2024. "Extracellular Vesicles as Human Therapeutics: A Scoping Review of the Literature." *Journal of Extracellular Vesicles* 13, no. 5: e12433. https://doi.org/10.1002/jev2.12433.

Gadella, T. W. J., L. Van Weeren, J. Stouthamer, et al. 2023. "mScarlet3: A Brilliant and Fast-Maturing Red Fluorescent Protein." *Nature Methods* 20, no. 4: 541–545. https://doi.org/10.1038/s41592-023-01809-y.

Gross, L. A., G. S. Baird, R. C. Hoffman, K. K. Baldridge, and R. Y. Tsien. 2000. "The Structure of the Chromophore Within DsRed, a Red Fluorescent Protein From Coral." *Proceedings of the National Academy of Sciences* 97, no. 22: 11990–11995. https://doi.org/10.1073/pnas.97.22.11990.

Herrmann, I. K., M. J. A. Wood, and G. Fuhrmann. 2021. "Extracellular Vesicles as a Next-Generation Drug Delivery Platform." *Nature Nanotechnology* 16, no. 7: 748–759. https://doi.org/10.1038/s41565-021-00931-2.

Hirosawa, K. M., Y. Sato, R. S. Kasai, et al. 2025. "Uptake of Small Extracellular Vesicles by Recipient Cells Is Facilitated by Paracrine Adhesion Signaling." *Nature Communications* 16, no. 1: 2419. https://doi.org/10.1038/s41467-025-57617-9.

Hung, M. E., and J. N. Leonard. 2016. "A Platform for Actively Loading Cargo RNA to Elucidate Limiting Steps in EV-Mediated Delivery." *Journal of Extracellular Vesicles* 5, no. 1: 31027. https://doi.org/10.3402/jev.v5.31027.

Ilahibaks, N. F., A. I. Ardisasmita, S. Xie, et al. 2023. "TOP-EVs: Technology of Protein Delivery Through Extracellular Vesicles Is a Versatile Platform for Intracellular Protein Delivery." *Journal of Controlled Release* 355: 579–592. https://doi.org/10.1016/j.jconrel.2023.02.003.

Jackson Cullison, S. R., J. P. Flemming, K. Karagoz, P. J. Wermuth, and M. G. Mahoney. 2024. "Mechanisms of Extracellular Vesicle Uptake and Implications for the Design of Cancer Therapeutics." *Journal of Extracellular Biology* 3, no. 11: e70017. https://doi.org/10.1002/jex2.70017.

Jenkins, P. M., M. He, and V. Bennett. 2015. "Dynamic Spectrin/Ankyrin-G Microdomains Promote Lateral Membrane Assembly by Opposing Endocytosis." *Science Advances* 1, no. 8: e1500301. https://doi.org/10.1126/sciadv.1500301.

Joshi, B. S., M. A. de Beer, B. N. G. Giepmans, and I. S. Zuhorn. 2020. "Endocytosis of Extracellular Vesicles and Release of Their Cargo From Endosomes." *ACS Nano* 14, no. 4: 4444–4455. https://doi.org/10.1021/acsnano.9b10033.

Kalluri, R., and V. S. LeBleu. 2020. "The Biology, Function, and Biomedical Applications of Exosomes." *Science* 367, no. 6478: eaau6977. https://doi.org/10.1126/science.aau6977.

Kathayat, R. S., and B. C. Dickinson. 2019. "Measuring S-Depalmitoylation Activity In Vitro and in Live Cells With Fluorescent Probes." In *Protein Lipidation: Methods and Protocols*, edited by M. E. Linder, (99–109). Springer. https://doi.org/10.1007/978-1-4939-9532-5_8.

Khuperkar, D., T. A. Hoek, S. Sonneveld, B. M. P. Verhagen, S. Boersma, and M. E. Tanenbaum. 2020. "Quantification of mRNA Translation in Live Cells Using Single-Molecule Imaging." *Nature Protocols* 15, no. 4: 1371–1398. https://doi.org/10.1038/s41596-019-0284-x.

Kim, I. S., S. Jenni, M. L. Stanifer, et al. 2017. "Mechanism of Membrane Fusion Induced by Vesicular Stomatitis Virus G Protein." *Proceedings of the National Academy of Sciences* 114, no. 1: E28–E36. https://doi.org/10.1073/pnas.1618883114.

Koontz, L. 2014. "TCA Precipitation." *Methods in Enzymology* 541: 3–10. https://doi.org/10.1016/B978-0-12-420119-4.00001-X.

Lai, C. P., E. Y. Kim, C. E. Badr, et al. 2015. "Visualization and Tracking of Tumour Extracellular Vesicle Delivery and RNA Translation Using Multiplexed Reporters." *Nature Communications* 6, no. 1: 7029. https://doi.org/10.1038/ncomms8029.

Lambert, G. G., H. Depernet, G. Gotthard, et al. 2020. "Aequorea's Secrets Revealed: New Fluorescent Proteins With Unique Properties for Bioimaging and Biosensing." *PLoS Biology* 18, no. 11: e3000936. https://doi.org/10.1371/journal.pbio.3000936.

Lee, J. A., J. Spidlen, K. Boyce, et al. 2008. "MIFlowCyt: The Minimum Information About a Flow Cytometry Experiment." *Cytometry Part A* 73A, no. 10: 926–930. https://doi.org/10.1002/cyto.a.20623.

Liang, X., D. Gupta, J. Xie, et al. 2025. "Engineering of Extracellular Vesicles for Efficient Intracellular Delivery of Multimodal Therapeutics Including Genome Editors." *Nature Communications* 16, no. 1: 4028. https://doi.org/10.1038/s41467-025-59377-y.

Liu, J., W. Li, X. Jin, F. Lin, J. Han, and Y. Zhang. 2023. "Optimal Tagging Strategies for Illuminating Expression Profiles of Genes With Different Abundance in Zebrafish." *Communications Biology* 6, no. 1: 1300. https://doi.org/10.1038/s42003-023-05686-1.

Ma, D., A. Xie, J. Lv, et al. 2024. "Engineered Extracellular Vesicles Enable High-Efficient Delivery of Intracellular Therapeutic Proteins." *Protein & Cell* 15, no. 10: 724–743. https://doi.org/10.1093/procel/pwae015.

McCann, J., C. D. Sosa-Miranda, H. Guo, et al. 2022. "Contaminating Transfection Complexes Can Masquerade as Small Extracellular Vesicles and Impair Their Delivery of RNA." *Journal of Extracellular Vesicles* 11, no. 10: e12220. https://doi.org/10.1002/jev2.12220.

McCullock, T. W., D. M. MacLean, and P. J. Kammermeier. 2020. "Comparing the Performance of mScarlet-I, mRuby3, and mCherry as FRET Acceptors for mNeonGreen." *PLoS ONE* 15, no. 2: e0219886. https://doi.org/10.1371/journal.pone.0219886.

Montecalvo, A., A. T. Larregina, W. J. Shufesky, et al. 2012. "Mechanism of Transfer of Functional microRNAs Between Mouse Dendritic Cells via Exosomes." *Blood* 119, no. 3: 756–766. https://doi.org/10.1182/blood-2011-02-338004.

Munis, A. M., E. M. Bentley, &, and Y. Takeuchi. 2020. "A Tool With Many Applications: Vesicular Stomatitis Virus in Research and Medicine." *Expert Opinion on Biological Therapy* 20, no. 10: 1187–1201. https://doi.org/10.1080/14712598.2020.1787981.

Munis, A. M., G. Mattiuzzo, E. M. Bentley, M. K. Collins, J. E. Eyles, and Y. Takeuchi. 2019. "Use of Heterologous Vesiculovirus G Proteins Circumvents the Humoral Anti-Envelope Immunity in Lentivector-Based In Vivo Gene Delivery." *Molecular Therapy—Nucleic Acids* 17: 126–137. https://doi.org/10.1016/j.omtn.2019.05.010.

Murk, J. L. A. N., G. Posthuma, A. J. Koster, et al. 2003. "Influence of Aldehyde Fixation on the Morphology of Endosomes and Lysosomes: Quantitative Analysis and Electron Tomography." *Journal of Microscopy* 212, no. 1: 81–90. https://doi.org/10.1046/j.1365-2818.2003.01238.x.

Obuchi, W., A. Zargani-Piccardi, K. Leandro, et al. 2025. "Engineering of CD63 Enables Selective Extracellular Vesicle Cargo Loading and Enhanced Payload Delivery." *Journal of Extracellular Vesicles* 14, no. 6: e70094. https://doi.org/10.1002/jev2.70094.

Parolini, I., C. Federici, C. Raggi, et al. 2009. "Microenvironmental pH Is a Key Factor for Exosome Traffic in Tumor Cells." *Journal of Biological Chemistry* 284, no. 49: 34211–34222. https://doi.org/10.1074/jbc.M109.041152.

Pemberton, J. G., T. Tenkova, P. Felgner, J. Zimmerberg, T. Balla, and J. Heuser. 2024. "Defining the EM-Signature of Successful Cell-Transfection." Preprint, bioRxiv, March 7. https://doi.org/10.1101/2024.03.07.583927.

Pizzey, A., C. Sutcliffe, J. C. Love, et al. 2025. "Exploiting the SunTag System to Study the Developmental Regulation of mRNA Translation." *Journal of Cell Science* 138, no. 6: jcs263457. https://doi.org/10.1242/jcs.263457.

Santos, M. F., G. Rappa, J. Karbanová, et al. 2021. "Itraconazole Inhibits Nuclear Delivery of Extracellular Vesicle Cargo by Disrupting the Entry of Late Endosomes Into the Nucleoplasmic Reticulum." *Journal of Extracellular Vesicles* 10, no. 10: e12132. https://doi.org/10.1002/jev2.12132.

Santos, M. F., G. Rappa, J. Karbanová, et al. 2023. "HIV-1-Induced Nuclear Invaginations Mediated by VAP-A, ORP3, and Rab7 Complex Explain Infection of Activated T Cells." *Nature Communications* 14, no. 1: 4588. https://doi.org/10.1038/s41467-023-40227-8.

Schindelin, J., I. Arganda-Carreras, E. Frise, et al. 2012. "Fiji: an Open-Source Platform for Biological-Image Analysis." *Nature Methods* 9, no. 7: 676–682. https://doi.org/10.1038/nmeth.2019.

Schipper, J. G., C. Aloise, S. O. Sutter, et al. 2025. "The Critical Role of Enterovirus 2A Protease in Viral Translation, Replication, and Antagonism of Host Antiviral Responses." Preprint, bioRxiv, Februarty 20. https://doi.org/10.1101/2025.02.20.639337.

Schnell, U., F. Dijk, K. A. Sjollema, and B. N. G. Giepmans. 2012. "Immunolabeling Artifacts and the Need for Live-cell Imaging." *Nature Methods* 9, no. 2: 152–158. https://doi.org/10.1038/nmeth.1855.

Soares, A. R., T. Martins-Marques, T. Ribeiro-Rodrigues, et al. 2015. "Gap Junctional Protein Cx43 Is Involved in the Communication Between Extracellular Vesicles and Mammalian Cells." *Scientific Reports* 5, no. 1: 13243. https://doi.org/10.1038/srep13243.

Somiya, M. 2020. "Where Does the Cargo Go?: Solutions to Provide Experimental Support for the 'Extracellular Vesicle Cargo Transfer Hypothesis." *Journal of Cell Communication and Signalingc* 14, no. 2: 173. https://doi.org/10.1007/s12079-020-00552-9.

Somiya, M., and S. Kuroda. 2021a. "Real-Time Luminescence Assay for Cytoplasmic Cargo Delivery of Extracellular Vesicles." *Analytical Chemistry* 93, no. 13: 5612–5620. https://doi.org/10.1021/acs.analchem.1c00339.

Somiya, M., and S. Kuroda. 2021b. "Reporter Gene Assay for Membrane Fusion of Extracellular Vesicles." *Journal of Extracellular Vesicles* 10, no. 13: e12171. https://doi.org/10.1002/jev2.12171.

Stewart, S. A., D. M. Dykxhoorn, D. Palliser, et al. 2003. "Lentivirus-Delivered Stable Gene Silencing by RNAi in Primary Cells." *RNA* (New York, N.Y.) 9, no. 4: 493–501. https://doi.org/10.1261/rna.2192803.

Stranford, D. M., L. M. Simons, K. E. Berman, et al. 2023. "Genetically Encoding Multiple Functionalities Into Extracellular Vesicles for the Targeted Delivery of Biologics to T Cells." *Nature Biomedical Engineering* 8, no. 4: 397–414. https://doi.org/10.1038/s41551-023-01142-x.

Tanaka, K. A. K., K. G. N. Suzuki, Y. M. Shirai, et al. 2010. "Membrane Molecules Mobile Even After Chemical Fixation." *Nature Methods* 7, no. 11: 865–866. https://doi.org/10.1038/nmeth.f.314.

Tanenbaum, M. E., L. A. Gilbert, L. S. Qi, J. S. Weissman, and R. D. Vale. 2014. "A Protein-Tagging System for Signal Amplification in Gene Expression and Fluorescence Imaging." *Cell* 159, no. 3: 635–646. https://doi.org/10.1016/j.cell.2014.09.039.

Tischer, C., A. Ravindran, S. Reither, N. Chiaruttini, R. Pepperkok, and N. Norlin. 2021. "BigDataProcessor2: A Free and Open-source Fiji Plugin for Inspection and Processing of TB Sized Image Data." *Bioinformatics* 37, no. 18: 3079–3081. https://doi.org/10.1093/bioinformatics/btab106.

Toribio, V., S. Morales, S. López-Martín, B. Cardeñes, C. Cabañas, and M. Yáñez-Mó. 2019. "Development of a Quantitative Method to Measure EV Uptake." *Scientific Reports* 9, no. 1: 10522. https://doi.org/10.1038/s41598-019-47023-9.

EV-TRACK Consortium. Van Deun, J., P. Mestdagh, P. Agostinis, et al. 2017. "EV-TRACK: Transparent Reporting and Centralizing Knowledge in Extracellular Vesicle Research." *Nature Methods* 14, no. 3: 228–232. https://doi.org/10.1038/nmeth.4185.

Van Niel, G., G. D'Angelo, and G. Raposo. 2018. "Shedding Light on the Cell Biology of Extracellular Vesicles." *Nature Reviews Molecular Cell Biology* 19, no. 4: 213–228. https://doi.org/10.1038/nrm.2017.125.

Wang, C., T. Zhao, Y. Li, G. Huang, M. A. White, and J. Gao. 2017. "Investigation of Endosome and Lysosome Biology by Ultra pH-Sensitive Nanoprobes." *Advanced Drug Delivery Reviews* 113: 87–96. https://doi.org/10.1016/j.addr.2016.08.014.

Welsh, J. A., D. C. I. Goberdhan, L. O'Driscoll, et al. 2024. "Minimal Information for Studies of Extracellular Vesicles (MISEV2023): From Basic to Advanced Approaches." *Journal of Extracellular Vesicles* 13, no. 2: e12404. https://doi.org/10.1002/jev2.12404.

Welsh, J. A., E. Van Der Pol, G. J. A. Arkesteijn, et al. 2020. "MIFlowCyt-EV: A Framework for Standardized Reporting of Extracellular Vesicle Flow Cytometry Experiments." *Journal of Extracellular Vesicles* 9, no. 1: 1713526. https://doi.org/10.1080/20013078.2020.1713526.

Yan, X., T. A. Hoek, R. D. Vale, and M. E. Tanenbaum. 2016. "Dynamics of Translation of Single mRNA Molecules In Vivo." *Cell* 165, no. 4: 976–989. https://doi.org/10.1016/j.cell.2016.04.034.

Zhang, X., Q. Xu, Z. Zi, et al. 2020. "Programmable Extracellular Vesicles for Macromolecule Delivery and Genome Modifications." *Developmental Cell* 55, no. 6: 784–801.e9. https://doi.org/10.1016/j.devcel.2020.11.007.

Zomer, A., S. C. Steenbeek, C. Maynard, and J. van Rheenen. 2016. "Studying Extracellular Vesicle Transfer by a Cre-loxP Method." *Nature Protocols* 11, no. 1: 87–101. https://doi.org/10.1038/nprot.2015.138.

Supporting Information

Additional supporting information can be found online in the Supporting Information section.

Supporting Figures 1–13: jev270228-sup-0001-figures.pdf **Supporting Video 1**: jev270228-sup-0002-Video1.avi **Supporting Table 1**: jev270228-sup-0003-Table1.pdf **Supporting Table 2**: jev270228-sup-0004-Table2.pdf **Supporting Table 3**: jev270228-sup-0005-Table3.pdf **Supporting Figure 1**: jev270228-sup-0006-SuppMat.docx